DESIGN, FABRICATION AND CHARACTERIZATION OF AN ULTRA-BROADBAND METAMATERIAL ABSORBER USING BISMUTH IN THE NEAR INFRARED REGION

A THESIS SUBMITTED TO
THE GRADUATE SCHOOL OF NATURAL AND APPLIED SCIENCES
OF
MIDDLE EAST TECHNICAL UNIVERSITY

BY

İMRE ÖZBAY

IN PARTIAL FULFILLMENT OF THE REQUIREMENTS
FOR
THE DEGREE OF MASTER OF SCIENCE
IN
ELECTRICAL AND ELECTRONICS ENGINEERING

SEPTEMBER 2018

Approval of the thesis:

DESIGN, FABRICATION AND CHARACTERIZATION OF AN ULTRA-BROADBAND METAMATERIAL ABSORBER USING BISMUTH IN THE NEAR INFRARED REGION

submitted by **İMRE ÖZBAY** in partial fulfillment of the requirements for the degree of **Master of Science in Electrical and Electronics Engineering Department, Middle East Technical University** by,

Prof. Dr. Halil Kalıpçılar
Dean, Graduate School of **Natural and Applied Sciences** _____

Prof. Dr. Tolga Çiloğlu
Head of Department, **Electrical and Electronics Eng.** _____

Prof. Dr. Gönül Turhan Sayan
Supervisor, **Electrical and Electronics Eng. Dept., METU** _____

Examining Committee Members:

Prof. Dr. Haluk Külah
Electrical and Electronics Engineering Dept., METU _____

Prof. Dr. Gönül Turhan Sayan
Electrical and Electronics Engineering Dept., METU _____

Assoc. Prof. Dr. Barış Bayram
Electrical and Electronics Engineering Dept., METU _____

Prof. Dr. Hamza Kurt
Electrical and Electronics Engineering Dept.,
TOBB University of Economics and Technology _____

Assoc. Prof. Dr. Alpan Bek
Physics Dept., METU _____

Date: _____

I hereby declare that all information in this document has been obtained and presented in accordance with academic rules and ethical conduct. I also declare that, as required by these rules and conduct, I have fully cited and referenced all material and results that are not original to this work.

Name, Last name :

Signature :

ABSTRACT

DESIGN, FABRICATION AND CHARACTERIZATION OF AN ULTRA-BROADBAND METAMATERIAL ABSORBER USING BISMUTH IN THE NEAR INFRARED REGION

Özbay, İmre
MSc., Department of Electrical and Electronics Engineering
Supervisor : Prof. Dr. Gönül Turhan Sayan

September 2018, 59 pages

In this study, the design-fabrication-characterization cycle of an ultra-broadband metamaterial absorber structure operating in the near infrared (NIR) is presented. The area of plasmonic metamaterial based broadband and ultra-broadband absorbers has been commenced less than ten years ago and such absorbers have quickly found applications in many areas including light harvesting, sensing, infrared imaging and very recently plasmonic hot electron mediated photochemistry. In this thesis, an ultrabroadband bismuth based metal-insulator-metal cavity absorber operating in the near infrared regime is presented. This is done together with a comprehensive literature review in conjunction with the relevance of the current work in literature. The device is composed of three layers (excluding the substrate that provides mechanical support) and the only layer requiring periodic lithographical patterning is the top layer which is patterned into nanodisks. Fourier Transform Infrared Spectroscopy (FTIR) measurements yield an absorption band of 800 nm -2400 nm. This makes the device suitable for microbolometer based infrared detection applications in most of the short wavelength infrared band (SWIR). The selection of materials and persistent optimization has lead to record breaking upper absorption edge to lower absoption edge ratio of 3:1 and a record breaking upper absorption wavelength edge to device thickness ratio of 10. Through using different techniques

such as using multiple patterning, the results and the operation bandwidth can be further improved.

Keywords: Plasmonics, Metamaterials, Metamaterial Based Absorbers, Broadband Absorbers

ÖZ

YAKIN KIZILÖTESİ BÖLGESİNDE ÇALIŞAN ÇOK GENİŞ BANTLI BİR METAMALZEME SOĞURUCUNUN BİZMUT KULLANILARAK TASARIMI, ÜRETİMİ VE KARAKTERİZASYONU

Özbay, İmre
Yüksek Lisans, Elektrik ve Elektronik Mühendisliği Bölümü
Tez Yöneticisi : Prof. Dr. Gönül Turhan Sayan

Eylül 2018, 59 sayfa

Bu çalışmada yakın dalga kızılötesi (NIR) bölgesinde işlevsel, çok geniş çalışma bandına sahip bir metamalzeme tabanlı sönümleyicinin tasarım-üretim-karakterizasyon döngüsü sunulmaktadır. Plazmonik metamalzeme tabanlı geniş veya çok geniş çalışma bandına sahip soğurucularla ilgili araştırmalar on yıldan daha kısa bir süre önce başlamıştır ve bu tür soğurucular ışıktan enerji hasatı, algılama, kızılötesi görüntüleme ve son zamanlarda da fotokimyasal süreçler gibi birçok uygulamada kısa sürede kendilerine yer bulmustur. Bu tezde metal-yalıtkan-metal kavite yapısında Bizmut metalinin kullanıldığı, yakın kızılötesi bölgesinde çalışan geniş bantlı bir soğurucunun tasarım, benzetim, üretim ve karakterizasyon (ölçüm) süreçleri sunulmaktadır. Bu sunum, yapılan çalışmanın literatürdeki yerini de kayda alan kapsamlı bir literatür taraması ile birlikte yapılmaktadır. Söz konusu cihaz üç katmandan (mekanik destek sağlayan alttaş tabakası haricinde) oluşmaktadır ve sadece, periodik bir nanodisk dizininden oluşan, en üst katman litografik desenleme sürecini gerektirmektedir. Fourier Transform Kızılötesi Speektroskopisi (FTIR) yöntemi ile yapılan ölçümler sonucunda cihazın 800 nm- 2400 nm bant aralığında çalıştığı saptanmıştır. Bu sayede, tasarlanan cihaz kısa dalga kızılötesi (SWIR) bandının büyük bir bölümünde mikrobolometre tabanlı kızılötesi tespit uygulamaları için faydalı olacaktır. Uygun malezeme seçimi ve itinalı geliştirme süreci ile, cihazın sönümleme bandı üst sınırı ile alt sınırı arasında 3’e 1’lik rekor seviyede bir oran

bulunmuştur. Ayrıca sönümleme bandı üst sınırı dalgaboyunun cihazın toplam kalınlığına oranının 10 olduğu tespit edilmiştir. Çoklu desenleme gibi farklı yöntemler kullanılarak sonuçların geliştirilmesi ve cihazın sönümleme bandının genişletilmesi mümkündür.

Anahtar Kelimeler: Plazmonik, Metamalzemeler, Metamalzeme Tabanli Sönümleyiciler, Geniş Bantlı Sönümleyiciler

To The Wind That Blows,

ACKNOWLEDGMENTS

The author would like to thank many who through their efforts, knowledge and support made the scientific outcome of this work possible.

First of all, the author acknowledges the support from his supervisor Prof. Dr. Gonul Turhan Sayan for her patience, guidance and time devoted besides all of her other duties. Her overall wisdom and her sharp eye for technical and official details have rendered this work possible in such a short amount of time. Without her presence, this thesis would not have made it to this realm.

Thanks from the author goes to every fellow of Bilkent University Nanotechnology Research Center (NANOTAM). The author would like to specifially (but not limited to) acknowledge the efforts of the following people:

-Dr. Bayram Butun, for being a substantial resource of supervision and support, being present for counseling whenever needed, even without official acknowledgement as a supervisor

-Amir Ghobadi, for his friendship and overall assistance especially during the measurement/characterization steps and perhaps most importantly for coming up with the material idea from where the author simply carried on

-Murat Gökbayrak, Ahmet Toprak and Ahmet Akbaş for their expertise during the fabrication steps of the final design and the not-so-much mentioned development processes for not-so-much successful devices.

-Mohsin Habib, for his help during the FTIR characterization of the final device (happy ending for an experimental work), and also for his aid some of which yielded not-that-happy endings.

The author apologizes for his forgetfulness towards anyone who further deserves mention but failed to find it in the text above.

TABLE OF CONTENTS

LIST OF FIGURES

FIGURES

CHAPTER 1

INTRODUCTION

1.1 Metamaterials

Metamaterials are sub-wavelength structured composite arrays that exhibit exotic optical properties which cannot be found in nature. In these design architectures, engineering light-matter interaction could lead to realization of variety of applications including light beaming, light confinement, and energy conversion. Unlike a bulk medium in which the inherent properties of the material are defined by the composition and electronic structure of the material, these sub-wavelength metamaterials obtain their response from the resonance conditions supported by the size, shape, and periodicity of the design. Thus, the optical response of the system can be broadly tailored by the use of proper design methodology. The ability of metamaterials to show strong magnetic responses at high frequency regimes, has opened door to realize several exotic properties. Unique phenomena including sub-wavelength imaging, negative refractive index, invisible cloak, perfect light absorption etc., that are impossible to be acquired with natural materials, have been demonstrated by carefully designing the unit cell for the specified frequencies. In such design structure, due to sub-wavelength dimensions of each unit, the incident light does not see the effect from single unit but rather the effect of overall average polarization and magnetization in the effective medium. Therefore, one can consider such periodic pattern of sub-wavelength elements as a medium with effective electric permittivity (($\varepsilon(\omega)$), and effective magnetic permeability (($\mu(\omega)$). Then the interaction of light and matter can be safely formulated by using the Maxwell equations. The differential form of Maxwell equations are given in a source-free medium as follow:

$$\nabla \times \vec{E} = -\frac{\partial \vec{B}}{\partial t} \quad (1.1) \qquad \nabla \times \vec{H} = \frac{\partial \vec{D}}{\partial t} \quad (1.2)$$

$$\nabla . \vec{D} = 0 \quad (1.3) \qquad \nabla . \vec{B} = 0 \quad (1.4)$$

where $\vec{E}$ is electric field (V/m), $\vec{H}$ is magnetic field (A/m), $\vec{D}$ is the electric field flux density (C/m^2), $\vec{B}$ is the magnetic field flux density (Wb/m^2). In a homogeneous and isotropic medium, these four parameters can be related to each other using below formula:

$$\vec{D} = \varepsilon \vec{E} \quad \& \quad \vec{B} = \mu \vec{H} \quad (1.5)$$

Thus, the equations (1.1)-(1.5) can be rewritten as;

$$\nabla \times \vec{E} = -\mu \frac{\partial \vec{H}}{\partial t} \quad (1.6) \qquad \nabla \times \vec{H} = \varepsilon \frac{\partial \vec{E}}{\partial t} \quad (1.7)$$

$$\nabla . \varepsilon \vec{E} = 0 \quad (1.8) \qquad \nabla . \mu \vec{H} = 0 \quad (1.9)$$

Assuming a time harmonic dependence for electric and magnetic fields, $\vec{E} = E_0 \, e^{-i\omega t}$ and $\vec{H} = H_0 \, e^{-i\omega t}$, the equations (1.6) and (1.7) can be reformed as:

$$\nabla \times \vec{E} = i\omega \mu \vec{H} \quad (1.10) \qquad \nabla \times \vec{H} = -i\omega \varepsilon \vec{E} \quad (1.11)$$

From here, the wave equation for a homogeneous and isotropic material can be defined as:

$$\nabla \times \left(\nabla \times \vec{E} \right) - k^2 \vec{E} = 0 \quad (1.12)$$

where k denotes the wave number and is equal to $k = nk_0$. In this formula k_0 is the free space wave number and n is the refractive index of the medium in which light propagates that is defined as $n = \sqrt{\varepsilon_r \mu_r}$ where $\varepsilon_r = {}^{\varepsilon}/_{\varepsilon_0}$, and $\mu_r = {}^{\mu}/_{\mu_0}$. According to the wave equation in (1.12), the signs of ε_r and μ_r defines the propagation and attenuation behavior of the wave inside the matter. In this context, materials can be classified as four different groups, as schematically shown in Fig. 1;

1. $\varepsilon_r > 0, \ \mu_r > 0$; This is the common response for most of materials. Insulators, semiconductors, and metals in frequencies above their plasma frequency represent this feature. If the relative permittivity assumes a real

value (which is the case for most of the insulators in visible light regime), light will propagate inside the layer without any attenuation. If permittivity has a complex value, in this case, the wave has both propagating and decaying natures. This is what we see for semiconductors in photon energies above their optical band gap.

2. $\varepsilon_r < 0,\ \mu_r > 0$; This class of materials is called as ε-negative (ENG) materials. This feature generally belongs to metals and highly doped semiconductors in the frequency regime below their plasma frequency. In this case, the value of $k^2 \sim n^2 < 0$ and therefore, the propagation vector has a large imaginary part and, it has a strong evanescent nature. The depth where light can propagate inside a metal is related to skin depth which depends on the amplitude of the real and imaginary parts of metal permittivity as well as the value of light frequency.
3. $\varepsilon_r < 0,\ \mu_r < 0$; This behavior has not been observed in any natural material. In this case, the light propagation is still possible but the direction of propagation vector is in the opposite direction to the direction of energy flow (that is in the direction of$\vec{E} \times \vec{H}$ vector) which means that the material is left handed. This property has been artificially acquired using metamaterials specifically in microwave frequency regime.
4. $\varepsilon_r > 0,\ \mu_r < 0$; This class of materials is called as μ-negative (MNG) materials. Similar to case 2, light intensity exponentiallydecays inside this medium and no propagating mode is supported with this type of materials. This phenomena has been recorded in some of ferromagnetic materials in microwave frequency range.

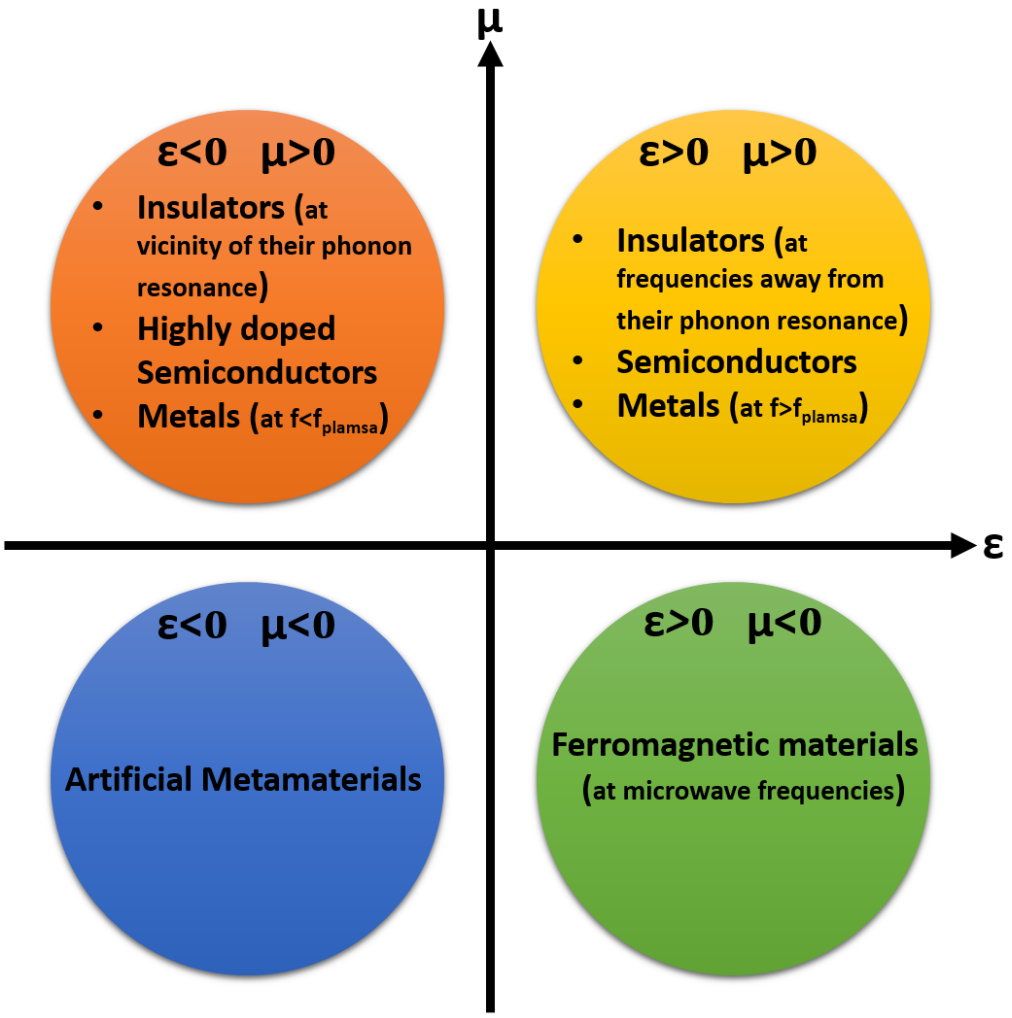

Figure 1. The classification of different materials based on the signs of their permittivity (ε) and permeability (μ).

1.2 Optical Properties of Metals

As shown in Fig. 2, the optical part of the electromagnetic (EM) spectrum can be divided into five main regions: ultraviolet (UV), visible (Vis), near infrared (NIR), mid infrared (MIR), and far infrared (FIR). Among all these frequency regimes, the Vis part (which spans from 400 nm to 700 nm) and NIR portion (from 700 nm- 5 μm), are of particular interest in optoelectronic, photovoltaic, and photo detection applications. The reason is the fact that about 97 percent of power produced by solar irradiation is located in this spectral regime. Hence, it is an essential requirement to efficiently harvest the light in these regimes. In this section, we will discuss the optical

properties of different type of materials and will compare their absorption mechanisms.

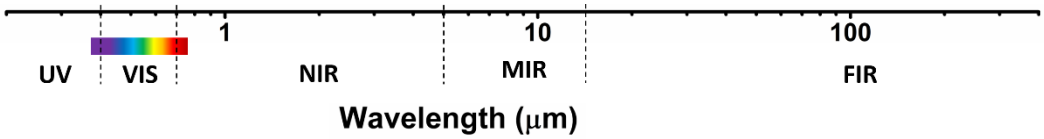

Figure 2. Classification of different portions of EM spectrum to five different wavelength regimes including UV, VIS, NIR, MIR, and FIR.

In general, materials can be divided into three main classes: 1) insulators (or so called dielectrics), 2) semiconductors, and 3) metals. Fig. 3 depicts the conduction and valance band positions for these three typical materials. Insulators have high optical band gap and therefore, they are transparent for Vis and NIR photons. Therefore, no absorption occurs in these materials and most of the light is transmitted. Semiconductors, however, have smaller optical band gap and can absorb photons with energies above their optical band gap. That's why, they can partially absorb the solar irradiation. Moreover, not only their optical band gap is important, the absorption coefficient is another factor that defines the strength of light absorption in semiconductor structures. Fig. 4 reveals the band gap and absorption coefficient of different semiconductor materials[1]. As this figure clearly implies, most of the semiconductors have optical band gap above 1.34 eV (which is the estimated optimal band gap for high efficiency optoelectronic and photovoltaic cells). This means that they can only absorb light in wavelengths below 1000 nm. But it should be considered that the high reflection value in these materials further limit their absorption efficiency. Most of these low band gap semiconductors have high refractive index (n) values which limits the amount of incident light energy penetrated into the

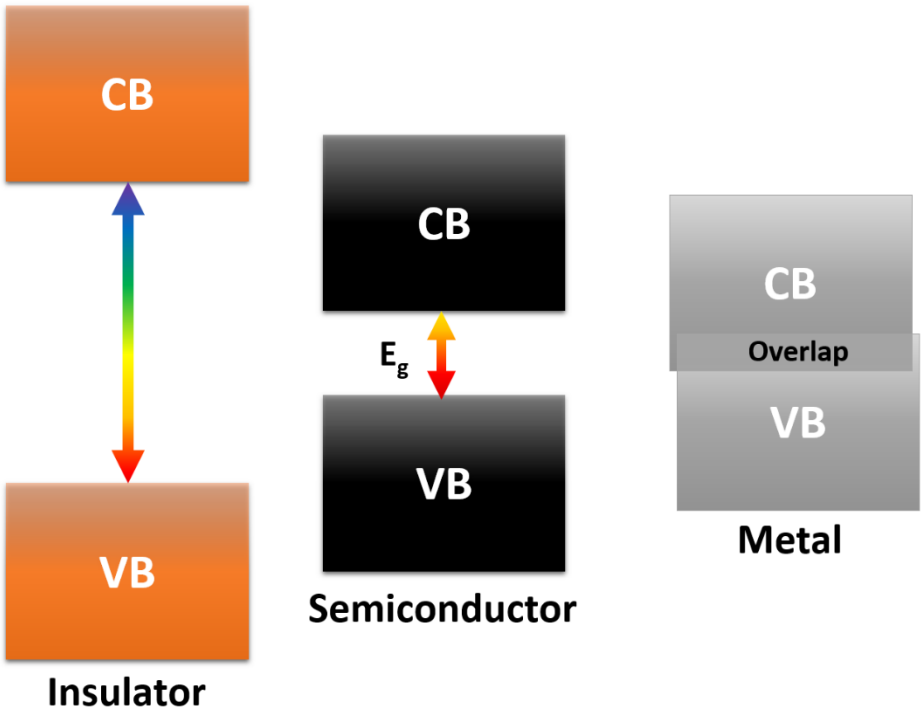

Figure 3. Absorption Mechanisms in three main materials of insulator, semiconductor, and metal

material. Therefore, further extension of light absorption toward longer wavelengths such as NIR range cannot be acquired using a semiconductor layer. Therefore, we need a material that can retain its absorption coefficient in longer wavelengths as well. The answer is metal layers. Metals, in their bulk form, are highly reflecting media that reflect most of the light. This is mainly due to their high permittivity values that only allows the incident light to penetrate inside the layer in an amount of its skin depth. Generally, metals are classified as two main categories; 1) noble metals such as gold (Au), and silver (Ag), and 2) lossy metals including nickel (Ni), titanium (Ti), chromium (Cr), and Tungsten (W). The noble metals have high values of permittivity and reflect back the most of NIR regime. While, real part of epsilon for lossy metals stays at small values around zero and by this way more light can be harvested compared to that of noble metals. A better qualitative comparison between loss characteristic of different metals can be acquired by calculation of their loss tangent. Loss tangent is the ratio between imaginary and real parts of permittivity. Fig. 5(a-c) shows the real part of permittivity, imaginary part of permittivity, and the loss tangent

for five different metals including; Au, Ni, Ti, W, and Bismuth (Bi). The permittivity data for Bi has been obtained by ellipsometry and the other metals are Plaik model[2]. As we can see from this figure, while noble metal such as Au takes an exponential drop toward large negative values while other

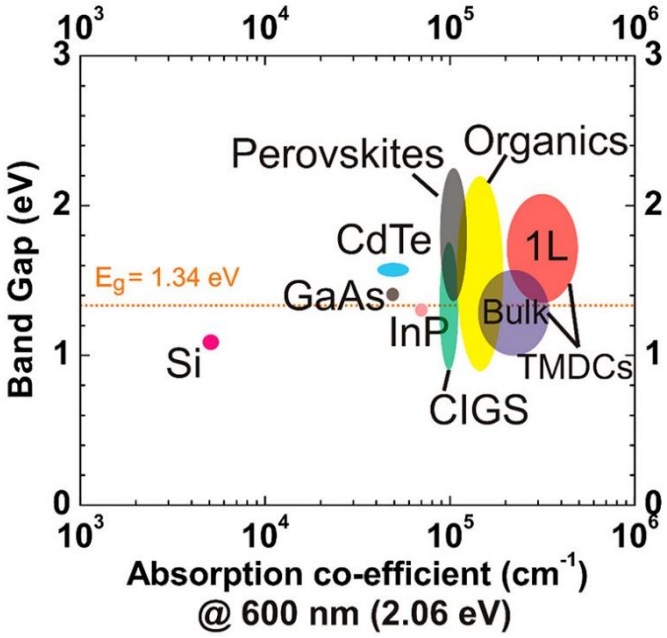

Figure 4. A comparison between the optical band gap and the absorption coefficient (at a specific wavelength range) for different types of semiconductors[1].

lossy metals keeps their small real part permittivity up to longer wavelengths. Among all, the largest loss tangent belongs to Ti and Bi. Moreover, an interesting feature is the response of Bi. As we can see, while all other metals eventually gets negative real permittivity, Bi gradually increases toward larger positive values as we go toward long wavelength NIR part of the spectrum. Therefore, it is envisioned that the use of these metals in a proper design configuration can lead to an efficient broadband perfect light absorption. Up to know, many studies have been devoted to realize light perfect absorbers using metal based metamaterials. These ideas can be generally classified into three main categories:

1. Metal-insulator-metal (MIM) cavity structures where the top metal layer is a nano patterned unit enabling light diffraction and its harvesting.

2. Planar, lithography free, Multilayer metal-insulator pairs $M(IM)_N$ based structures that acquire light perfect absorption in a broad frequency range by introducing impedance matched conditions

3. Metal based three dimensional (3D) trapping scaffolds such as nanowires, or nanocones in which the light perfect absorption is achieved by gradual matching of the air impedance into underlying absorbing design.

Considering the fact that this thesis explores the planar sub wavelength absorbers, the third group would not be investigated in detail. Next chapter, we will provide a theoretical background on the design configurations and operation mechanisms used for achieving light perfect absorption in broadband sub-wavelength planar light perfect absorbers.

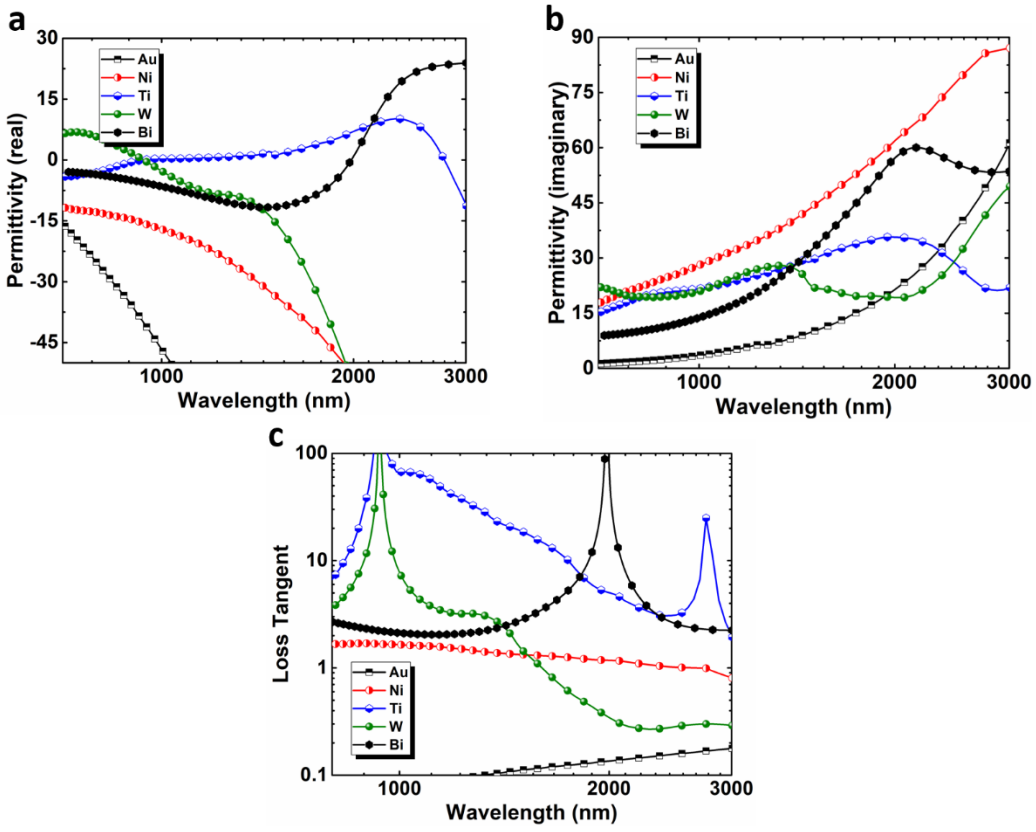

Figure 5. The (a) real part of permittivity, (b) imaginary part of permittivity, and (c) loss tangent for different Nobel and lossy metals.

1.3 Metamaterial Based Perfect Light Absorbers

Metamaterials are a type of artificial materials that are made of properly designed inclusions with exotic optical properties. Negative refraction[3]–[5], artificial magnetism[6], [7], asymmetric transmission[8], [9], lasing[10], [11], cloak of invisibility[12]–[14], and sub-wavelength light absorption[15] are some examples of these mentioned attributes. The light harvesting by the use of nanostructured designs has turned into an intensively explored areas, recently. Efficient absorption of the incoming light employing a lossy medium such as metal, or semiconductor can make the near unity light harvesting possible. These metamaterial based perfect absorbers have many potential applications. Metal based ones can show their absorption behavior in broad or narrow wavelength regimes. The narrowband counterparts are of special attention in imaging, sensing, and filtering applications[16]–[24]. While the metal based broadband absorbers are essentially needed in thermal photovoltaics[25]–[27], radiative cooling[28]–[30], hot electron based photodetectors[31], [32], photochemistry[33], and efficient solar vapor/steam generation[34]–[36] applications. Moreover, these ultrathin light harvesting optical devices can be realized in semiconductors in which an efficient light confinement can cause near unity light harvesting and this in turn can exceed the Yablonovitch limit in an ultrathin thickness[37]. Furthermore, generation of a high density of photo induced carriers in an ultra-small semiconductor thicknesses could boost their collection chance. In last years, these semiconductor metasurfaces and metamaterials have been utilized in variety of potential applications such as photovoltaics, photodetectors, and other optoelectronic devices [31], [38]–[49]. These perfect absorbers have also been realized in other types of materials, such as polar and two dimensional (2D) materials.

1.4 Thesis Motivation

The efficient harvesting of electromagnetic (EM) waves using ultra small sub-wavelength nano designs would lead to perfect absorption of light. These perfect absorbers have wide variety of applications, including sensing, filtering, photovoltaic and thermal photovoltaics, and photodetection. Advances in nanofabrication have

provided the opportunity to observe strong light-matter interaction in various optical nanostructures. Therefore, in recent decade, the concept of metamaterial based light perfect absorbers has gained a lot of attention in all wavelength regimes. This thesis explores the material and architecture requirements for the realization of light perfect absorption using the multilayer metamaterial design approaches for our particular interest of near infrared (NIR) regime. We provide a general theoretical formulation to find the ideal condition for achieving near unity light absorption in a simple metal-insulator-metal (MIM) design. Later, these theoretical estimations are compared with the permittivity data of different metals to find the optimum material for light perfect absorption. Our findings prove the extraordinary response of the Bi in the NIR regime to obtain light near perfect absorption from 800 nm to 2400 nm which is the highest absorption bandwidth (BW) reported up to know. This, in turn, shows the importance of the choice of material together with the right configuration to maximize the light absorption BW. In the rest of the thesis, we first provide a theoretical background on the physical mechanisms responsible for light perfect absorption in different metamaterial device perfect absorbers. Later, based on the findings of this section, we design and simulate a Bi based MIM structure for operation in NIR regime. Finally, the fabrication route and characterization results are provided in detail. In the last part, we conclude this thesis with briefly explaining the future work and direction of this thesis.

CHAPTER 2

BACKGROUND

2.1 Broadband Metal Based Light Perfect Absorber

This section provides a literature survey on the use of different design architectures for realization of broadband light perfect absorption.

2.1.1 MIM Cavity based perfect absorbers

The most intensively investigated metal based metamaterial for perfect light absorption is based on sub-wavelength metal-insulator-metal (MIM) cavity [17], [23], [50]–[58]. In this MIM architecture, the top metal layer is a nano unit plasmonic noble metal while the bottom layer acts as an ideal mirror that reflects the light back into the cavity. In the abovementioned architecture, the incident light is efficiently coupled to cavity modes and collective oscillation of electrons in top nanostructured metal through the surface plasmon resonances (SPRs) excitation can lead to near unity light harvesting in a specific wavelength value [23], [56]. However, owing to the fact that the SPRs excitation is generally narrow, the bandwidth (BW) of these plasmonic devices are spectrally narrow [15], [51], [53], [59]–[73]. A wide variety of architectures are utilized to extend the absorption BW of the plasmonic based MIMs. The use of multi-dimensions/shapes for the top metal layer is one of the most frequently studied ideas for broadening the BW. These structures are designed in a fashion that the superposition of different SPR modes could lead to overall ultra-broadband light perfect absorption [52], [74]–[81]. For a patch unit lying on the (x-y) plane with width and length of W_x and W_y, the resonance frequency can be estimated as[77]:

$$\lambda_R = \frac{2\sqrt{\varepsilon_i}}{\sqrt{(l/W_{xeff})^2+(m/W_{yeff})^2+(k_{zi}/\pi)^2}} \quad (1.13)$$

where the ε_i is the permittivity of the insulator layer, l and m are the integers that shows the supported mode number, W_{xeff} and W_{yeff} are the effective length and width of the patch considering the fringing field of the patch, and $k_{zi}$is the z component of the wave vector inside the insulator layer and it is found using:

$$k_x^2 + k_y^2 = k_i^2 + k_{zi}^2 \quad (1.14)$$

According to this formula, the position of the resonance frequency can be tuned by altering the width and length of the patch. Therefore, the proper use of multiple but close dimensions can provide us a multi resonant system. Now, according to the spectral width of each of these resonance frequencies, we can get a multiband or flat broadband absorber. The width of a resonance frequency is compared by a parameter called, quality factor (Q). Q is the ratio between the spectral position of the resonance wavelength and the full-width-at-half-maximum (FWHM) BW of the layer. This factor, in turn, depends on the damping constant of the metal. The simplest analytic equation that define the permittivity of a plasmonic metal is the Drude-Lorentz-Sommerfeld relation:

$$\varepsilon_M(\omega) = \varepsilon_0 - \omega_P^2/(\omega^2 + i\gamma\omega) \quad (1.15)$$

where ε_0 is the effective permittivity of the metal that describes the contribution of bound electrons, ω_P is the plasma frequency of the metal which differs from metal to metal and generally located at Vis and UV regimes, ω is the frequency of the incident light, and γ is the damping constant of electron motion. Generally, this constant is bigger for lossy metals compared to that of plasmonic ones. That's why, it can be deduced that the use of lossy metals instead of a plasmonic noble metal can lead to a broader absorption response. It is demonstrated that the use of Cr, and Ti have provided an ultra-broadband light absorption. Back to equation (1.13), we can see that the dimension of the unit defines the resonance frequency of the design. The use of an elongated structure with two major and minor axis dimensions such as ellipse or rectangle can lead to two different resonance frequencies. Analogous to antenna

theory, this structure is similar to two monopole antennas with different effective lengths that have two different resonance modes. Therefore, one can extend light absorption by using this design strategy.

2.1.2 Lithography Free MI Pairs Based Perfect Absorbers

As discussed in previous section, to obtain light perfect absorption in a MIM cavity design, the top metal layer should support SPR modes. To have this feature, therefore, these units need to be at sub-wavelength geometries. These ultra-small nanostructures can be fabricated using electron beam lithography (EBL) which is essentially an improper tool for up scaling of the design. Thus, in recent years, the concept of non-resonant widely impedance matched MI pairs based multilayers has attracted much attention. These perfect absorbers can be made by multiple deposition processes and do not need any lithography step [82]–[110]. Unlike the above-mentioned resonant plasmonic metamaterial absorbers, non-resonant $M(IM)_N$ pairs based multilayers that are composed of lossy/noble metals can be employed to realize ultra-broadband near unity light harvesting in the Vis and NIR regions [90], [111]. To be able to have an understanding the limits of these designs, we can utilize transfer matrix method (TMM), to find the ideal model for light perfect absorption. In fact, we look for an ideal material named X in the MIX configuration. The proposed structure is depicted in Scheme. 1. In this notation, M, I, and X stand for thick metal reflector, spacer insulator, and ideal absorber medium. Using the analytical-numerical TMM method, we can extract the ideal condition in which light will be fully harvested in an ultra-broadband wavelength regime. For this aim, we consider a multilayer design. In every layer, we have forward and backward propagating waves. Assuming that the incident light polarization is transverse magnetic (TM), the equations are written for the y-directed component of the magnetic field (H_y). If we want to solve this equation for TE polarization, then same equations are valid for x-directed component of the magnetic field (E_x). The H_y inside every layer can be formulated as follows [111]:

$$H_y(z)=\begin{cases} A_t e^{ik_A(z-D_X)}+A_r e^{-ik_A(z-D_X)}, & z>D_X \\ M_{11}e^{ik_X z}+M_{12}e^{-ik_X z}, & 0<z<D_X \\ D_1 e^{ik_I z}+D_2 e^{-ik_I z}, & -D_I<z<0 \\ M_{21}e^{ik_M(z+D_I)}+M_{22}e^{-ik_M(z+D_I)}, & -D_I-D_M<z<-D_I \\ S_t e^{ik_S[z+(D_I+D_M)]}, & z<-D_I-D_M \end{cases} \} (1). \qquad (1.16)$$

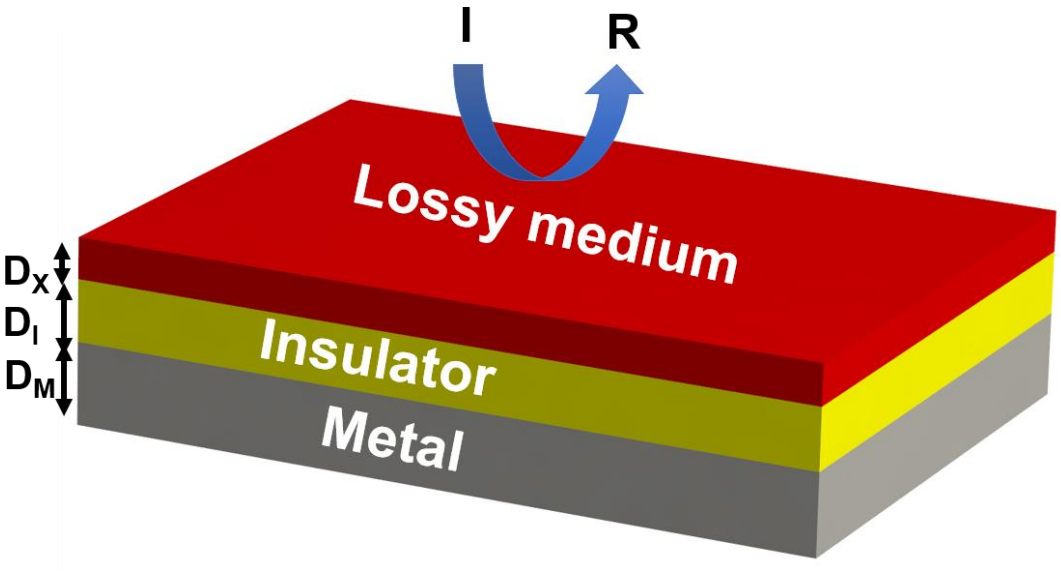

Scheme. 1. Schematic representation of the studied MIX design to find the ideal condition for light perfect absorption.

Where $k_{j=(a,X,I,M,s)}=\sqrt{\varepsilon_j\omega^2/c^2-k_x^2}$. In these formulations, D_I, D_X, and D_M are the thicknesses of the dielectric, lossy medium and bottom metal reflector layers, respectively. c is the speed of light in vacuum, k is the wave number inside different media, and ε is the permittivity data of different layers. Applying the boundary conditions for transverse magnetic (TM) polarization (the continuity of the fields and their derivatives at the boundaries separating different media), reflection of the incident light from the structure can be obtained as $R=|F_{12}/F_{11}|^2$. Here, $F=\begin{bmatrix} F_{11} \\ F_{12} \end{bmatrix}=a^{-1}m_{11}m_{12}^{-1}d_1d_2^{-1}m_{21}m_{22}^{-1}s$ where

$$a=\begin{bmatrix} 1 & 1 \\ ik_A/\varepsilon_A & -ik_A/\varepsilon_A \end{bmatrix},\ s=\begin{bmatrix} 1 \\ ik_S/\varepsilon_S \end{bmatrix}, \quad (1.17)$$

$$m_{11}=\begin{bmatrix} 1 & 1 \\ ik_X/\varepsilon_X & -ik_X/\varepsilon_X \end{bmatrix},\ m_{12}=\begin{bmatrix} e^{ik_X D_X} & e^{-ik_X D_X} \\ ik_X e^{ik_X D_X}/\varepsilon_X & -ik_X e^{-ik_X D_X}/\varepsilon_X \end{bmatrix}, \quad (1.18)$$

$$d_1=\begin{bmatrix} 1 & 1 \\ ik_I/\varepsilon_I & -ik_I/\varepsilon_I \end{bmatrix},\ d_2=\begin{bmatrix} e^{ik_I D_I} & e^{-ik_I D_I} \\ ik_I e^{ik_I D_I}/\varepsilon_I & -ik_I e^{-ik_I D_I}/\varepsilon_I \end{bmatrix}, \quad (1.19)$$

$$m_{21}=\begin{bmatrix} 1 & 1 \\ ik_M/\varepsilon_M & -ik_M/\varepsilon_M \end{bmatrix},\ m_{22}=\begin{bmatrix} e^{ik_M D_M} & e^{-ik_M D_M} \\ ik_M e^{ik_M D_M}/\varepsilon_M & -ik_M e^{-ik_M D_M}/\varepsilon_M \end{bmatrix}, \quad (1.20)$$

In these formula, ε_M is the bottom metal layer permittivity, $\varepsilon_I$is the insulator layer permittivity, and ε_X is the permittivity data to obtain the perfect light absorption. Taking into account the normal direction of light incidence and the planar shape of the design, the same results are hold for transverse electric (TE) polarization. Knowing the permittivity and thickness of the bottom metal and insulator layers together with the top X layer thickness, we can theoretically obtain the real and imaginary values of ε_X in which the absorption stays about 0.9 that is the condition for near unity for perfect light absorption. In fact, the reflection contour plot as a function of real and imaginary parts of epsilon has been obtained using a MATLAB code. The contour plot is made of centric circles that shows the boundaries for reflections of 0.1, 0.2, and so on. To be able to obtain a reflection below 0.1, we need to stay inside the $R=0.1$ circle. The upper and lower values of this circle define the acceptable range of data for real part of epsilon. The right and left values also show the acceptable range of permittivity values for imaginary part.

In this design architecture, the highly absorbing lossy medium (which has a thickness in the order of several nanometers) should satisfy the impedance matched conditions in a broad frequency range of our interest. To gain a better view on the limitations of this design, the proposed TMM equations (1.16-1.20) are adjusted for an MIX cavity to explore the permittivity values of an ideal material. In the proposed modelling, the metal layer in bottom is an optical mirror and the insulator is set as SiO_2. The ideal range of real and imaginary permittivity values, to achieve an absorption above 0.9, are extracted for different X layer thicknesses of 5 nm, and 15 nm where the spacer layer thickness is fixed at 100 nm. Taking the absorption BW threshold as 0.9, if the

permittivity data of a material in a specific wavelength is located inside the highlighted range, it can ensured that light perfect absorption has been achieved. As shown in Fig. 6, thinner ideal layer thicknesses can provide wider tolerable ranges for near unity light absorption. However, thicker ones shift the bottom edge of the tolerable region toward zero. These extracted ideal cases have been compared with the permittivity data of other metals such as Au, Cr, Ti, Ni and W. As depicted in Fig. 6(a-d), the tolerable permittivity range becomes positive as we go to longer λs. However, almost all type of metals (including both noble [Au] and lossy ones [W, Cr, Ti]) have large negative real permittivity values in large wavelengths such as NIR. Therefore, in a MIM planar design, the light perfect absorption is restricted to wavelengths below 1000 nm. This could be broadened to larger λs by tuning the effective permittivity of the metals through its composition with a lower index medium [111]–[113]. Recently, a method based on the dewetting was adopted to synthesize sub wavelength random sized nanoholes in an ultrathin Cr coating to tune its overall permittivity [111]. It was demonstrated that this strategy can broaden the absorption upper edge from 850 nm (for planar

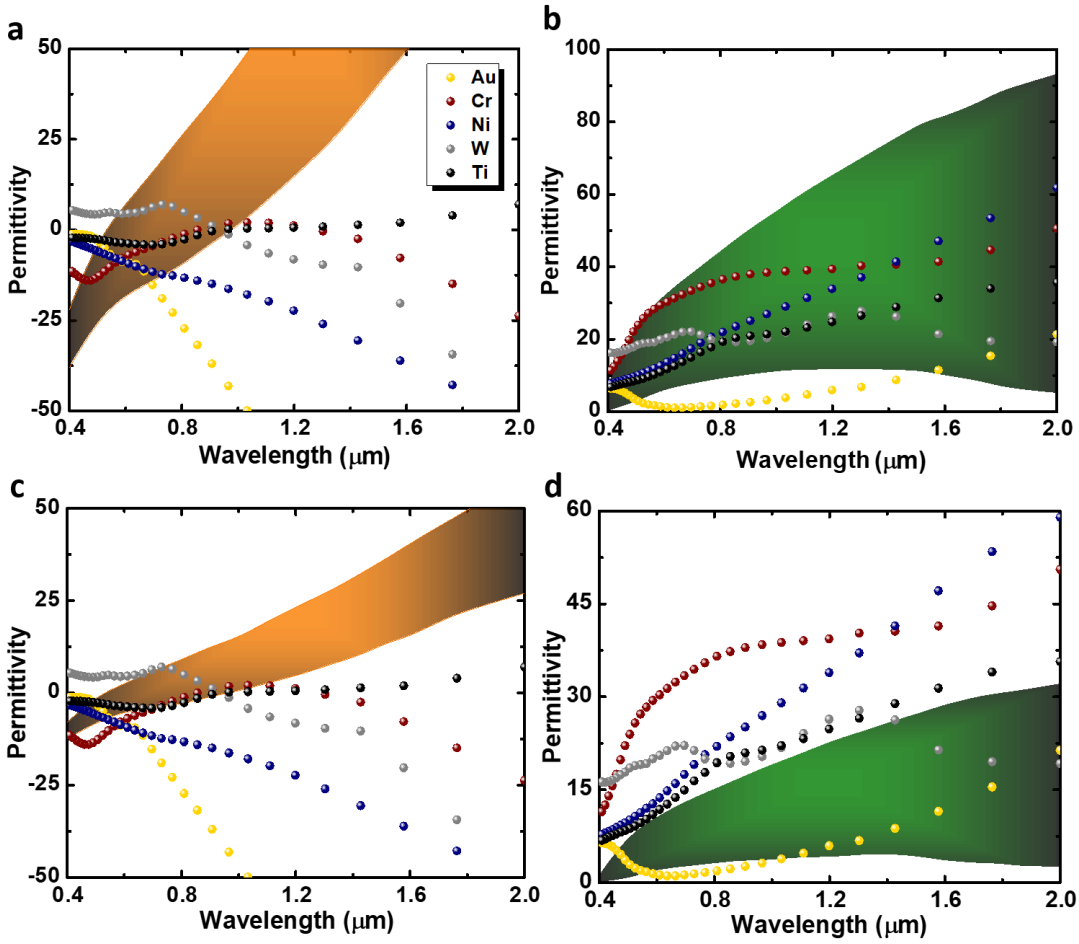

Figure 6. Comparison between the permittivity data of different metals and the ideal data of a MIM perfect absorber. (a) The real and (b) imaginary parts of permittivity for the case of D_I =100 nm, D_M =5 nm. (c) The real and (d) imaginary parts of permittivity for the case of D_I =100 nm, D_M = 15 nm. The brawn and green highlighted regions show the range of permittivity values for real and imaginary parts of permittivity in which a reflection below 0.1 can be attained. In a specific wavelength, if both real and imaginary parts of a metal stays inside these regions, an absorption above 0.9 can obtained.

design) to 1150 nm (for dewetted nanohole design). Furthermore, the control in metal deposition could also lead to formation of multi-shape designs and by this way, a broader absorption response can be achieved compared to planar design [113].

According to above mentioned data, the MIM architecture has inherent absorption BW limit and the extension of its absorption BW needs to a right selection of the material. Different from other common types of metals, Bismuth (Bi) has positive real part of permittivity in large wavelengths. Therefore, it is expected that it can nicely matched to our ideal model. For this aim, we replace the spacer with Alumina and get the ideal

material data for three different cases: 1) D_I =120 nm, D_M =5 nm, 2) D_I =150 nm, D_M =5 nm, and 3) D_I =120 nm, D_M =10 nm. These ideal data has been compared with those of permittivity values of Bi. As we can see from Fig. 7, the matching is great for the Bi in the MIM configuration.

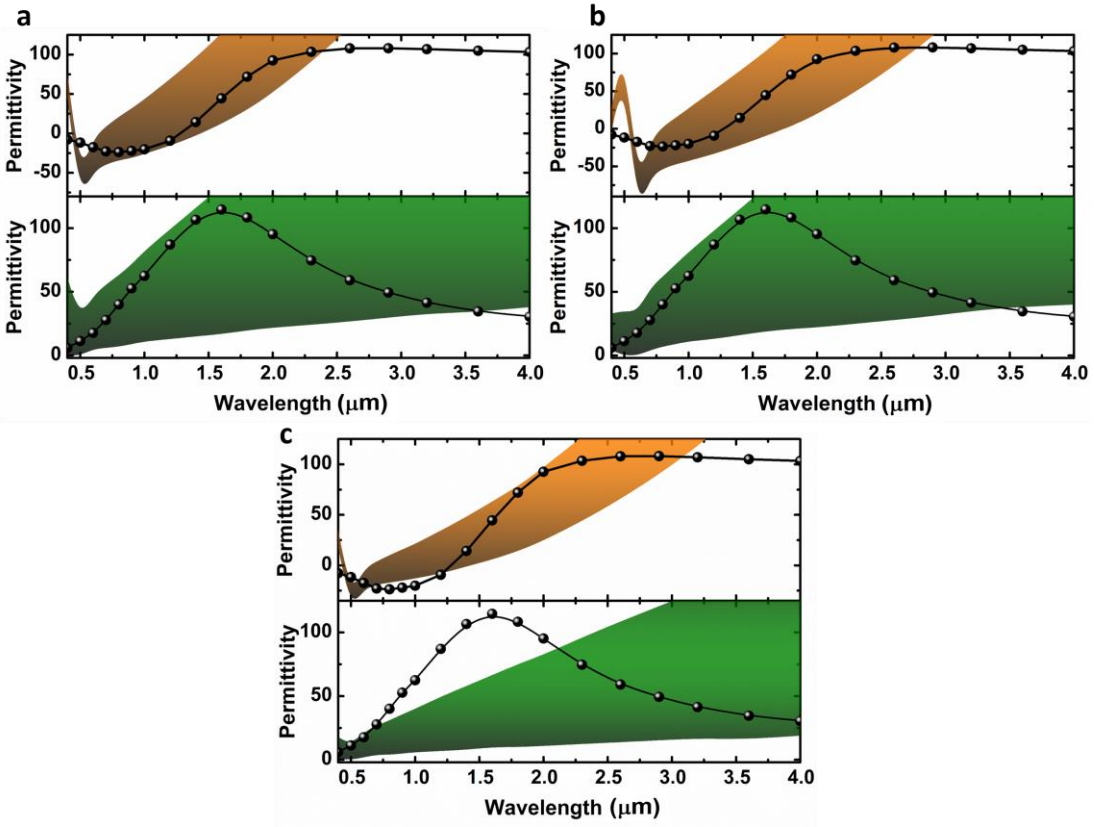

Figure 7. Comparison between the permittivity data of Bi and the ideal data of a MIM perfect absorber. for three different cases of (a) D_I =120 nm, D_M =5 nm, (b) D_I =150 nm, D_M = 5 nm, and (c) D_I =120 nm, D_M = 10 nm. Similar to previous case, the highlighted regions show the tolerable permittivity values to obtain above 0.9 absorption. The brown region belongs to real part and green is related to imaginary portion.

This absorption BW could be substantiated using a metal-insulator-metal-insulator (MIMI) architecture. Same as MIM cavity, the ideal region is extracted for two case of D_I =100 nm, D_M =5 nm, and D_I =100 nm, D_M =15 nm. These data have been compared with all different metals permittivity values. Fig. 8 reveals the real and

imaginary parts of permittivity for different metals and compared them with the ideal near unity perfect absorber model.

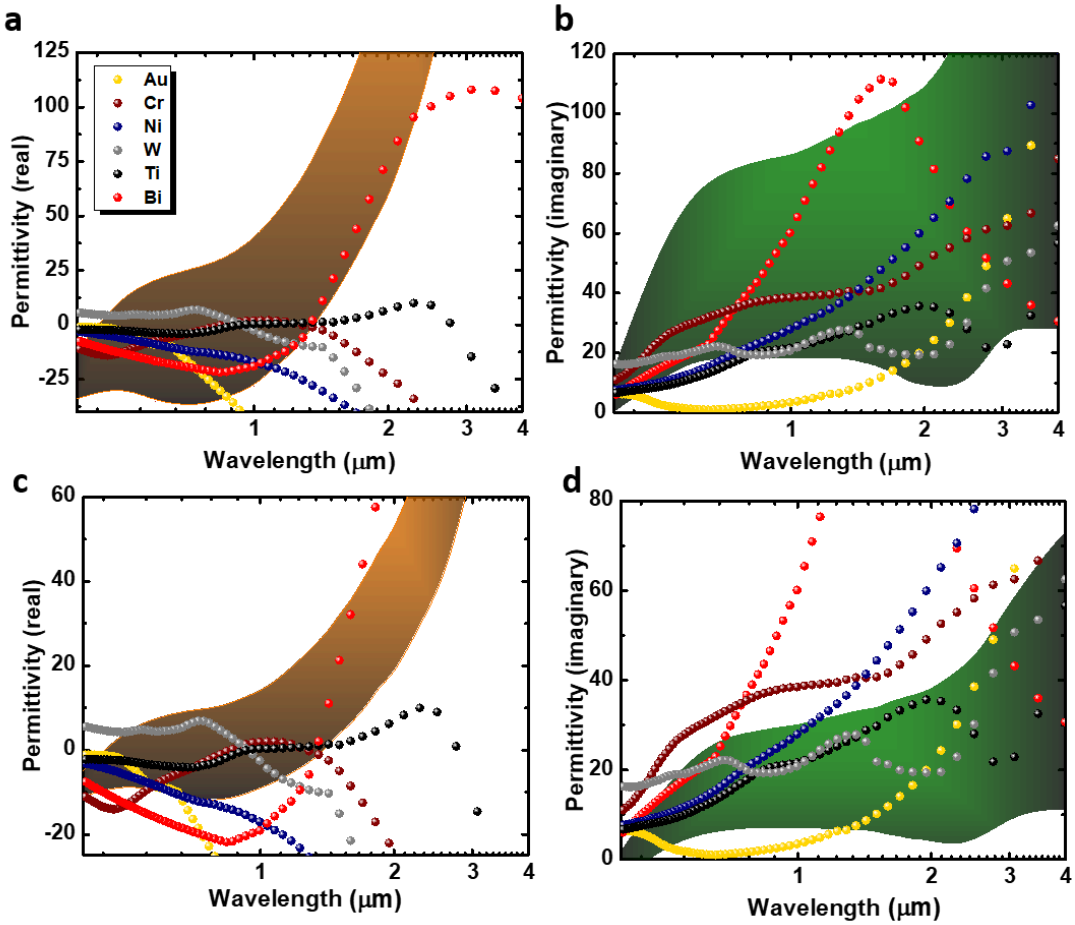

Figure 8. Comparison between the permittivity data of different metals and the ideal data of a MIMI perfect absorber. (a) The real and (b) imaginary parts of permittivity for the case of D_I =100 nm, D_M =5 nm. (c) The real and (d) imaginary parts of permittivity for the case of D_I =100 nm, D_M = 15 nm. The ideal region (in which an absorption above 0.9 is guaranteed) is highlighted with brown and green.

In the MIMI structure, the top most insulator coating operates as a broad antireflecting layer which provides a gradual match among the air and bottom MIM cavity impedances. Looking at the ideal data for this case, it can be deduced that the absorption BW has been enlarged in comparison with MIM design) [93], [95], [101]–[103]. However, same as MIM structure, the extension of light absorption toward MIR frequencies cannot be attained by this architecture. Although scaling the number of pairs to higher values could further increase the absorption BW but again the upper edge is yet restricted to the NIR regime [95], [98]–[100]. Increasing the insulator layer

thickness will red-shift both the lower and upper absorption edge in which the perfect light absorption will not cover the visible region[89]. Previously, It was demonstrated that 16 pairs Ni/SiO_2 and Ti/SiO_2 (where the metal layer thickness is in the order of 1-2 nm) could support near unity absorption up to 2.5 μm[98]. However, such high number of layers could add substantial complexity into the fabrication of the design. Therefore, improvement in the BW while taking the device dimensions ultrathin is of particular interest. To attain this, different strategies have been introduced. The optimum choice of back reflector[103], multi-thickness metal layers[101], and incorporation of randomly sized nano holes[102] can further improve the absorption BW in MIMI configuration. The right arrangement of various multilayers with properly designed thicknesses can also be used to achieve the impedance matched condition[114]. Similar to MIM design, Bi could have been nicely matched to this deisgn. As illustrated in Fig. 8, Bi real permittivity in visible regime has low negative values and becomes positive as we go toward longer wavelengths. Hence, it can be expected that by altering the thicknesses of insulator and Bi layers in an MIM or MIMI design, near unity absorption can be achieved in an ultra-broadband wavelength range. To demonstrate this fact, the ideal tolerable region is extracted for the case of D_M = 5 nm, and D_I = 150 nm and its matching is compared with that of permittivity data of Bi and Ti (as two metals that have positive permittivity values in long wavelengths). As it can be understood from this data, the perfect absorption of light is kept up to 3 μm with the MIMI design. Thus, besides the absorber design configuration, the proper selection of the material is also vital to achieve perfect light absorption in an ultra-broadband frequency range. It should be said that the common methodology for near unity light harvesting in these metamaterial based multilayers throughout NIR and MIR regimes is to use tapered scaffolds[99], [115]–[122]. However, these designs suffer from complex lithography and etching steps. Moreover, some other studies realized perfect light absorption by the integration of ultrathin metal with lithography free light trapping [123], [124] Recently, it was demonstrated that a 10 nm thick Pt layer coated on randomly grown TiO_2 nanowires can harvest above 97% of incoming light in a broad frequency range covering the Vis and the NIR regime[123].

CHAPTER 3

DESIGN AND SIMULATION

The geometry used in our design has been explored and exploited by other authors [50]. However the results obtained in this work have been unparalleled and this achievement is not only due to pure optimization, but rather a systematic study of material properties and correct choice of materials. In this section, material analysis and data fitting leading to optimization of the design will be discussed. This section is classified as follows;

3.1. Simulation Domain and Design Geometry

3.1.1 Boundary Conditions

3.1.2 Excitation and Spectra

3.2. Parametric Optimization: The Impact of Different Geometries

3.3. Fields Distribution Analysis

The geometry or at least the topology of our design can be expressed as a metal-insulator-metal (MIM) structure with the top metal layer patterned into circular disks as shown in Fig. 9. The structure supports resonant plasmonic modes on the top metal layer and the bottom metal layer. Although both of these modes are dissipative and are the main source of absorption, they differ in nature as the top layer modes are mainly local and the bottom layer modes are mainly propagating. Both modes require numerical solvers for their analysis. For this purpose, Lumerical FDTD Solutions was used. Compared to finite element solvers that work in frequency domain which need to run separate simulations for each frequency, FDTD has the significant advantage of running broadband simulations in a single run. This feature is especially important for the design of ultra-broadband absorbers as the name suggests.

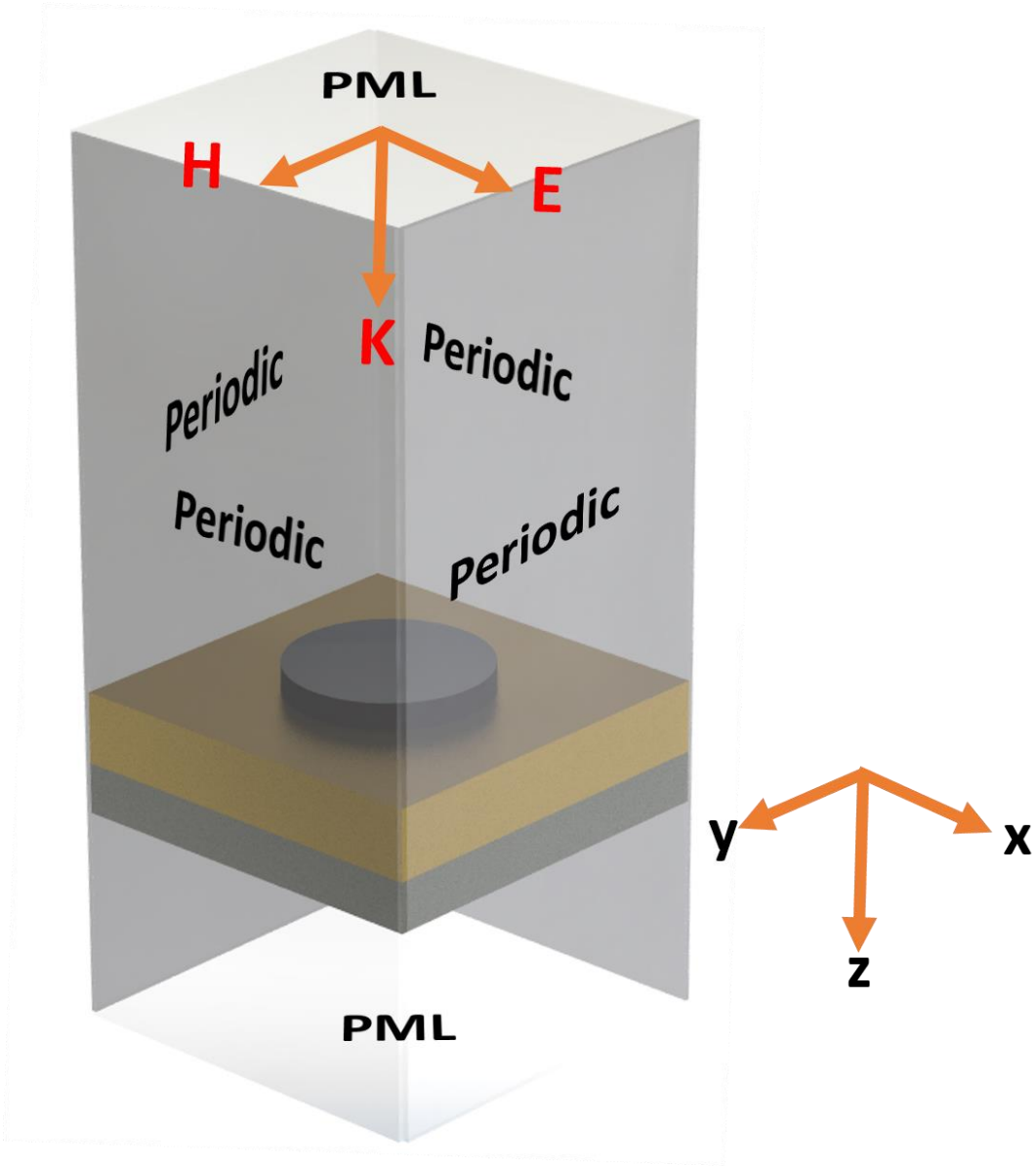

Figure 9. The simulation domain and the boundary conditions utilized to simulate the proposed MIM structure

3.1 Geometry and Simulation Domain

3.1.1 Boundary Conditions:

The rectangular unit cell has 6 edge surfaces. These are positive and negative surfaces for all three Cartesian components x, y and z and the simulation domain is terminated at these edges of the unit cell. Appropriate boundary conditions are required here.

Lumerical FDTD Solutions provide 6 different boundary conditions for the edges.

***Perfectly matched layer (PML)*:** This is a reflectionless boundary condition. The name comes from the fact in electromagnetics that matched regions do not reflect waves while unmatched regions reflect waves based on the degree of mismatch. Regions can correspond to two separate transmission lines on a device level as well as an air region or a dielectric region on a three dimensional propagation problem. This boundary condition mimics the walls of an anechoic chamber through numerical means. The boundaries absorb the incoming electromagnetic waves incident on them and does not reflect back into the structure within the simulation domain. This is achieved through adding several (typically 8 to 10) layers on the outer part of the surface with gradually increasing dissipation. The gradual change prevents the waves from reflecting back and the dissipation absorbs the waves.

Metal or Perfect Electric Conductor (PEC): This boundary condition acts as a perfect electric conductor. For such surfaces, the electric field component parallel to the surface and the magnetic field component perpendicular to the surface are forced to be zero. This yields a perfectly reflecting boundary condition, not letting any power to escape the simulation domain from the given surface.

Perfect Magnetic Conductor (PMC): This is the magnetic equivalent of the PEC condition. The magnetic field component parallel to the surface and the electric field perpendicular to the surface are forced to be zero, creating the condition for a perfect reflection. It should be noted that while PEC can be experimentally realized to a great extent using metals, PMC boundary condition is not experimentally realizable.

Periodic Boundary Condition: When both the electromagnetic fields and structures are periodic, this condition can be used. Depending on the nature of periodicity, this condition can be applied in one, two or three axes. Based on the structural and electromagnetic periodicity, the two ends of the simulation domain are ‘connected’ through this boundary condition. Contrary to other boundary conditions, this condition applies to both positive and negative sides on the same axis. If positive X side is chosen to be periodic, same applies to negative X side.

Bloch Boundary Condition: This is an extension of the periodic boundary condition. A periodic structure is analyzed when the field involves a phase difference between the unit cells of the periodic structure. This boundary condition is particularly used for oblique excitation of the structure.

Symmetric/Anti-Symmetric Boundary Condition: When a problem (both structure and source) exhibits a plane of symmetry, this boundary condition can be used. Symmetric boundary condition acts as a mirror for the electric field and anti-mirror for the magnetic field. Anti-symmetric boundary condition acts as a mirror for the magnetic field and an anti-mirror for the electric field.

In this thesis, two boundary conditions, the PML and Periodic type are used as depicted in Fig. 9 in describing the unit cell of the absorber. As the absorber structure is periodic in x and y directions with an infinite extent, the periodic boundary condition is applied on the surfaces of the unit cell which are perpendicular to x and y axes.

3.1.2 Excitation and Spectra:

The simulation starts by the design of a time pulse excitation using a plane wave source to synthesize a proper pulse spectrum. Then, the designed time domain pulse is launched into the simulation domain. Since the simulation domain is periodic in x and y directions, the source geometry needs to be so as well.

Throughout this study, various pulses with similar yet different spectra were used. The final and most widely used pulse will be described here.

A pulse with an initial offset of 11.31 fs and pulse length of 3.99 fs was used corresponding to a Gaussian spectrum in frequency domain or a skewed Gaussian in wavelength domain.

In wavelength domain, the pulse was designed to span from 700 nm to 3000 nm. This range was picked due to the spectrum of interest, numerical considerations and the available data for the materials. Material data was not available above 3000 nm and although exciting the system with an even broader spectrum was possible, it was not preferred.

3.2 Parametric Optimization: The Impact of Different Geometries

After the material data acquisition and model fitting are complete, simulation domain with sources and structures are defined; simultaneous simulations are run and the optimization starts. The whole design procedure involves many iterations and detours some of which will be omitted here, and the converging results around the final design will be demonstrated.

To begin with, we need to geometrically optimize our design to achieve the maximum absorption BW. For this aim, the commercial finite-difference time-domain (FDTD) software package (Lumerical FDTD Solutions)[125] is exploited to numerically simulate the optical performance of the designed absorber. The unit cell shown in Fig. 9 is excited with a broadband time pulse spanning the spectrum from 800 nm to 3000 nm in desired polarization and incidence angles. The boundary conditions (BCs) in x and y directions are chosen as periodic BCs while the bottom and top BCs are set as perfectly matched layer (PML). In general, the absorption A of a system can be found using the formula of $A = 1 - R - T$ where R is the effective reflection coefficient and T is the effective transmission coefficient computed for the structure. Considering the fact that the bottom layer is an optically thick mirror with almost no transmission, we can safely say that there is zero transmittance in this device. Therefore, the absorption spectra can be calculated directly from reflection spectra using the formula, $A = 1 - R$. For this aim, the reflection monitor is placed on top of the incident source excitation plane to only collect the reflected wave. The proposed MIM structure is excited and reflection data is collected.

To maximize the absorber design performance, three main geometries should be optimized; spacer insulator layer thickness (D_I), nanodiscs metal layer thickness (D_M), and their corresponding radius (R). As proved in previous studies[102][126], the lower absorption edge of an MIM (or MIMI) design is tuned using the spacer layer thickness. In fact the absorption in lower wavelength range is controlled with the path supported with MIM cavity. In the other words, increasing the cavity length will lead to a red shift in the lower absorption edge. Increasing the spacer thickness will expose a red

shift in the lower absorption edge. Choosing 0.9 as the absorption threshold of our design, the insulator layer thickness is swept from 100 nm to 160 nm (with a step of 10 nm), in a way that the lower absorption edge is located in the spectral position of λ = 800 nm. This is the beginning of the NIR region. The D_M and R values are fixed at 20 nm and 200 nm, during this simulations. As shown in Fig. 10(a), as we go toward larger insulator layer thicknesses, the upper and lower absorption edges experience red shift. For instance, in the case of insulator layer thickness of 100 nm, the perfect light absorption is covered up to 1050 nm while this coverage starts from 900 nm and continues up to 2350 nm. However, our goal is to extend the upper absorption edge while keeping the lower edge at the 800 nm. Looking in the absorption spectra for different insulator layer thicknesses, it can be found that the lower BW edge can be placed at around 800 nm by choosing the D_I in a value between 140 nm and 150 nm. At this case, the upper edge is located at a value around 2200 nm. Thus, the optimum value for spacer layer thickness is picked as 145 nm. In the next step, we further optimize the design. For this aim, similar sweep is applied for the nanodisc height (D_M) to explore the impact of this geometry in the absorption response of the MIM design. Generally speaking, the thickness of this nanoresonant unit plays a crucial role in the absorption strength and BW of the design. If the thickness of the nano unit is too thick, then the light cannot pass through it and consequently the response of the top plasmonic layer dominates the cavity response. On the other hand, if we use too thin layers, the strength of the cavity modes becomes quite weak in which we cannot have efficient coupling of the incident light into the cavity modes. Therefore, a moderate value is required to have the best optical absorption response. As illustrated in Fig. 10(b), increase in the thickness of nanodisc resonator shifts the upper absorption edge toward longer wavelength values while the lower edge is almost unchanged (as expected). As already mentioned, the top nanoresonator tailors the strength of cavity modes and controls the coupling of incident wave to collective oscillation of top metal electrons via the excitation of surface plasmon resonances (SPRs) which in

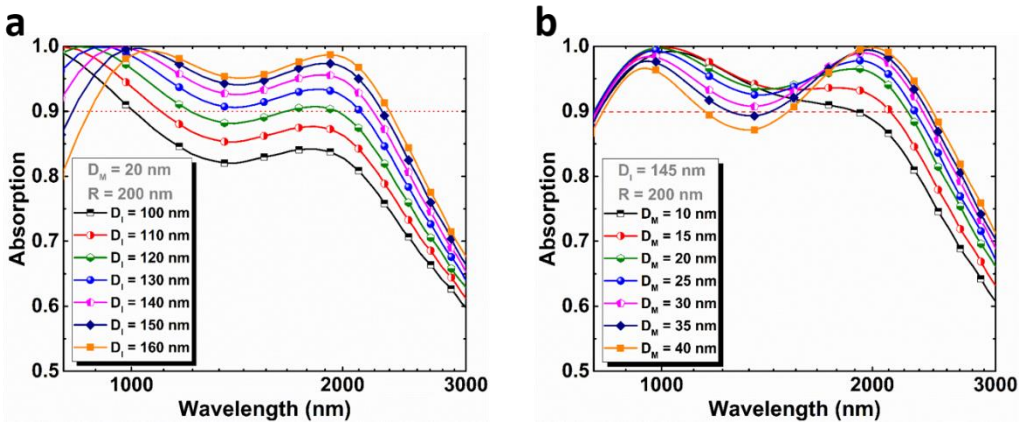

Figure 10. The absorption spectra for different sweeps on (a) insulator thickness (D_I), (b) top metal thickness (D_M).

turn leads to light harnessing in the designed frequency range. As shown in the figure, moving toward thicker D_M layers, the upper band peak strengthen while the one in shorter wavelengths loose its strength. Therefore, a moderate designed thickness could provide us a fair trade-off between these two factors. The spectra has two local peaks at the low and high wavelengths. In the case of disc height of 10 nm, the second peak (the one located at longer wavelengths) is quite weak. This is expected as we already told that the upper peak is influenced with the strength of the cavity modes. An absorption above 0.9 is attained in the range of 800 nm- 2300 nm for $D_M = 25$ nm, and 810 nm- 2350 nm for $D_M = 30$ nm, respectively. This shows a step forward in maximizing the absorption BW of the design. Another parameter left for investigation is the radius of the nanodisc. Finally, to maximize absorption BW of the absorber,design the radius of nanodisc resonator should be tuned. For this purpose, the insulator layer is fixed at 145 nm and a sweep on R is conducted from 180 nm to 200 nm for two different D_M values of 25 nm and 30 nm. The absorption spectra of these different design configurations have been depicted in Figs 11(a-b).

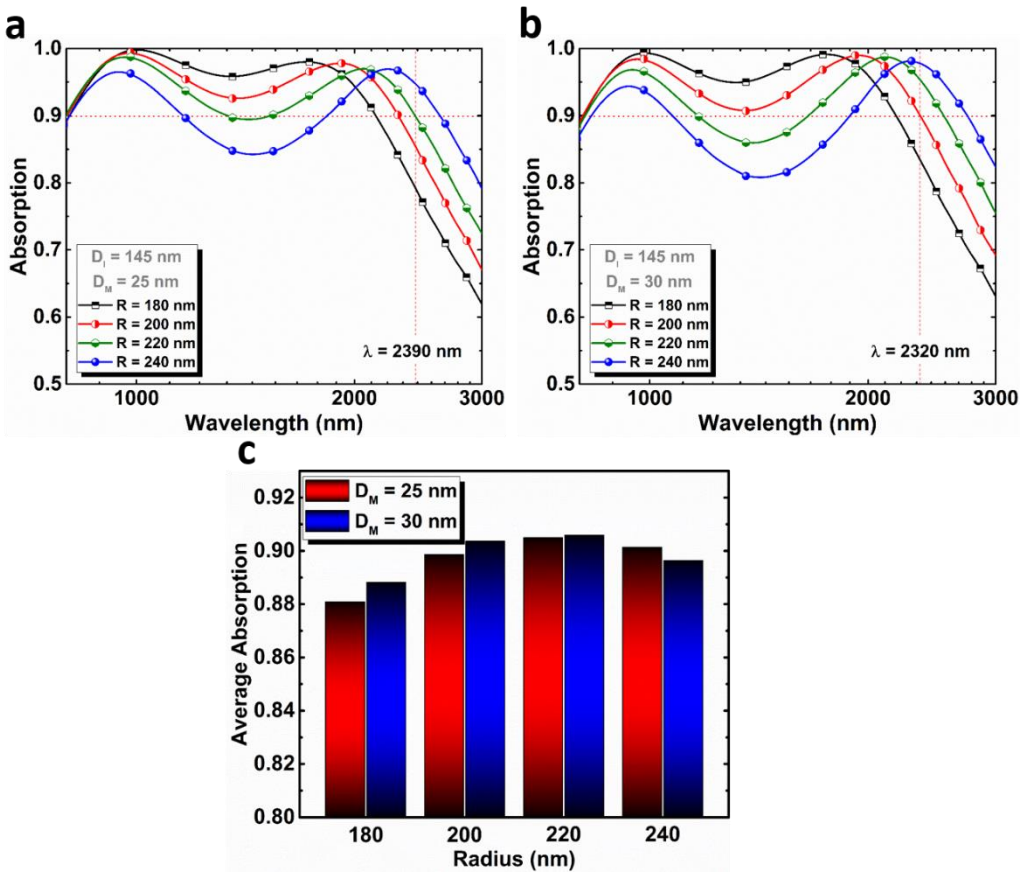

Figure 11. The absorption spectra for different sweeps on (a,b) the radius of the nanodiscs (R). (c) The average absorption has been calculated for different design geometries

As shown in these panels, increasing the disc radii will induce a red shift in the spectral position of the second resonance. This can be explained taking the antenna terminology into consideration where these nanodiscs can be considered as a monopole antenna. As the size of the resonator increases the resonance wavelength moves to longer values. The nature of this phenomenon will be further scrutinized in the following sections. To have a better qualitative comparison, the average absorption in our desired wavelength regime (800 nm- 3000 nm) have been calculated using following formula:

$$\text{Average Absorption} = \frac{\int_{800}^{3000} \alpha(\lambda)\, d\lambda}{\int_{800}^{3000} \lambda\, d\lambda} \tag{3.1}$$

where α is absorption coefficient and λ is the incident light wavelength. Based on the data in Fig. 11(c), it can be shown that the average absorption above 0.9 is achieved in three different design configurations; $D_M = 25$ nm & $R = 220$ nm, $D_M = 30$ nm &

$R = 200$ nm, $D_M = 30$ nm & $R = 220$ nm. Among these three geometry sets, $D_M = 25$ nm & $R = 220$ case has the largest absorption BW. This design can retain absorption above 0.9 in an ultra-broadband wavelength range of 800 nm- 2390 nm. Therefore, as the consequence of our numerical simulations the optimal design parameters are $D_I = 145$ nm, $D_M = 25$ nm, and $R = 220$ nm. To the best of our knowledge, this is the broadest reported MIM absorber operating in the optical frequency ranges. Moreover, the overall thickness of the design is in the order of $\sim\lambda/10$ (here λ corresponds to the upper edge of the absorption bandwidth) that follows from the extraordinary permittivity function of Bi metal.

3.3 Fields Distribution Analysis

After optimizing design parameters, the origin of this ultra-broadband light absorption is investigated. This could be achieved by examining the electromagnetic field distributions through the MIM cavity at different wavelength values. For this goal, the electric field (E-field) and magnetic field (H-field) distributions are computed in two resonance wavelengths of 960 nm and 2060 nm which were computed for the optimal perfect absorber that we examined in the previous section. The view plane cuts through all three layers of MIM cavity as shown in Fig. 12(a). The excitation pulse has transverse magnetic (TM) polarization, as exhibited in this panel. The same results hold for the case of transverse electric (TE) polarization, considering the fact that the proposed design is a bare planar design with infinite fold symmetry. Figures 12(b-c) present the plots of the E-field distribution for two resonance wavelengths of 960 nm and 2060 nm, respectively. As shown in this figure, both resonances are essentially the electric dipole resonances excited on the nanodisks along the *x*-axis where the E-field is mainly concentrated in the walls of disks. However, the H-field distributions have

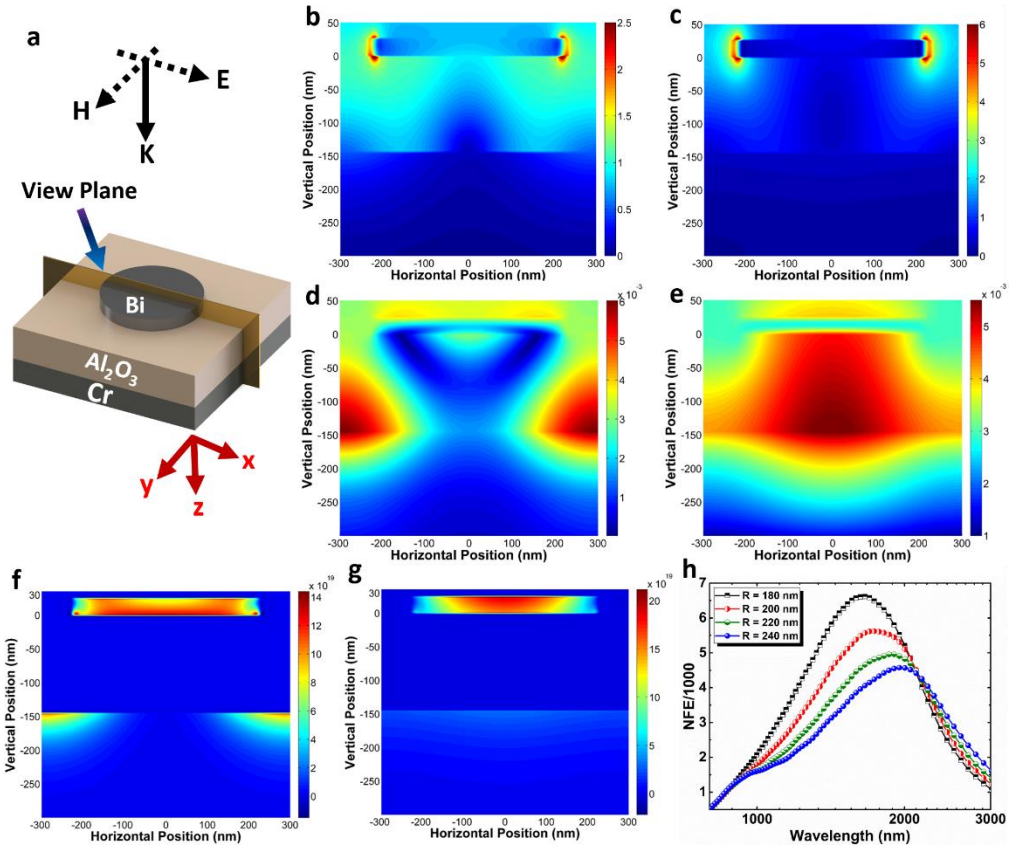

Figure 12. (a) Schematic representation of the view plane in the MIM cavity design. The E-field distributions in the resonance peak spectra positions of (b) 960 nm, and (c) 2060 nm. The H-field distributions in the resonance peak spectra positions of (d) 960 nm, and (e) 2060 nm. The calculated absorption profiles inside the cavity absorber in the resonance peak spectra positions of (f) 960 nm, and (g) 2060 nm. (h) The NFE profile for four different nanodisc radii of 180 nm, 200 nm, 220 nm, and 240 nm.

distinct differences. As shown in Fig 12(d), the H-field is mostly confined inside the cavity and between the nanodiscs. While, this confinement is much stronger in beneath of discs for the case of longer wavelength resonance as shown in Fig. 12(e). Based on the findings of previous studies [127], the shorter wavelength resonance ($\lambda = 960$ nm) is due to coupling of incident wave into propagating surface plasmons (PSPs) which propagate in the interface of spacer and continuous bottom layer; while the localized surface plasmons (LSPs) tare confined below the nanounit resonator. However, the localized field in the case of $\lambda = 2060$ nm proves the dominancy of LSPs underneath of Bi patches. To evaluate this statement, we have calculated the absorption profile inside the cavity using the below formula:

$$A(\lambda) = 0.5\omega\, imag(\varepsilon)|E|^2 \quad (3.2)$$

where ω is the angular frequency, imag(ε) is the imaginary part of complex permittivity of the layer (Bi or Cr) and $|E|$ is the amplitude of E-field in a specific point. The calculated absorption profiles have been exhibited in Figs 12(f-g) for two resonance wavelengths of 960 nm, and 2060 nm, respectively. As it can be clearly seen from this figure, the light harvesting in shorter resonant mode has occurred in both top nanodisc and bottom continuous layer. The fact that absorption in bottom layer is concentrated in between the discs which verifies our findings that the first mode is partially originated from PSPs. Looking at the profile in longer wavelength peak resonance, we can say that the light is almost fully harvested in the top layer. In fact the localized field between bottom mirror and top nanodisc is consumed by both layers, but due to much more lossy nature of the Bi (compared to Cr) in longer wavelengths, most of the power is absorbed in top Bi nanodisc. Furthermore, to get insight on the impact of nanodisc radius in the strength and spectral position of second resonance, the near field enhancement (NFE) is calculated for different nanodisc radii. NFE is defined as $|E|^2$ where $|E|$ is monitored at top nanodisc-insulator interface in the intersection point of view plane and the circular circumference. As revealed in Fig. 12(h), the NFE has a Gaussian like distribution with a peak that matches to the spectral position of second absorption resonance. At smaller disc radii, the peak of NFE is stronger and moving toward larger discs. The spectral position of this peak experiences a red-shift while the peak amplitude gradually drops. Therefore, up to some point, increasing the lateral size of nanodisc can provide near unity absorption in longer wavelengths which in turn makes the BW wider. In fact, the position of the second resonance should be chosen in a way that superposition of this absorption peak with the shorter wavelength mode can lead to an overall near unity absorption. Larger radius amounts will decouple these two peaks and a dip starts to appear between these two modes as shown in Figs 11(a-b).

CHAPTER 4

FABRICATION AND CHARACTERIZATION

This section provides a detailed information on the fabrication tools employed for fabrication of the proposed MIM perfect absorber and briefly discusses their operation principles. As shown in Fig. 13, the proposed design is composed of a bottom Cr metal layer which is 100 nm thick to completely block the light transmission. The spacer layer is a 145 nm thick Al_2O_3 layer which was found to be the optimized thickness for the spacer layer. The top patch is Bi nanodiscs with a thickness of 25 nm. The top view of a unit cell of the design has been also provided in this figure.

4.1 Fabrication

4.1.1 Sample Cleaning

In order to fabricate this design, in the first step, we need to clean the substrate. For this purpose, standard Silicon wafer cleaning process in applied into the sample. First of all, the Silicon substrate is diced into 1.5 cm*1.5 cm pieces using dicer tool. The used Silicon wafer had a growth direction of (111), an unintentional doping, and the top side of it was polished. To start the cleaning process, we first prepared a strong acid solution to remove the organic residues on the sample. The prepared chemical is called Pirahna. Pirahna is a strong organic solver which is made of mixture containing hydrogen peroxide (H_2O_2) and sulfuric acid (H_2SO_4) with a ratio of 3 to 1. After mixing these chemicals inside a container, the solution is left for 5 min to make sure that it is in thermodynamic equilibrium. Afterward, the Silicon substrate pieces are placed inside the solution to remove the organic pollutants on the surface of the sample. The samples are hold in the container for a duration of 5 min. Afterward, the sample is taken out of the solution and washed with deionized (DI) water couple of

times to make sure that the chemical is removed completely from the sample. Then sample is then placed inside hydrofluoric (HF) acid which is a dangerous acid

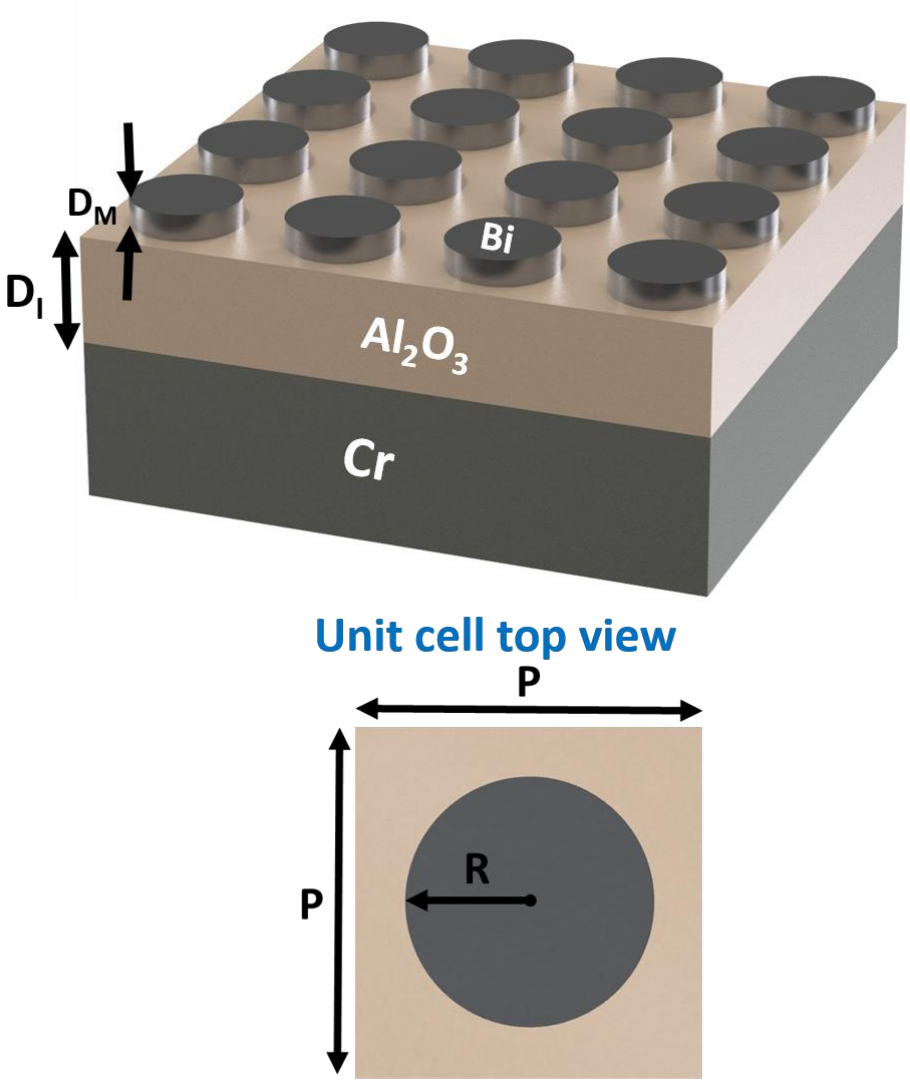

Figure 13. The proposed MIM design which is made of Cr-Al_2O_3-Bi nanodiscs and its corresponding top view.

which removes the native metal oxides which is SiO_2 in our case. Since HF is a strong metal oxide etchant, the duration of HF dip is taken as 30 seconds which is quite enough to remove the oxidized ultrathin top layer. Then sample is again washed with water couple of times to make sure that all residues and chemicals are removed. Finally, the sample is dried with nitrogen (N_2) blow. It should be mentioned that during the wet bench process, all safety issues were considered to remove any potential risk

raised from acid solutions. The use of Neoprene gloves, and safety glasses was a part of these precautions. At the end of the process samples are placed back into the petry dish and immediately they were prepared to put into thermal evaporation chamber for the next step.

4.1.2 Thermal Evaporation

In general, deposition systems can be classified as two main categories: 1) chemical vapor deposition (CVD), and physical vapor deposition (PVD). İn PVD process, the target film is physically deposited on the sample and there is no strong chemical bond between the substrate and film. However, in CVD process, the deposition is realized using a gaseous source which can uniformly coat the substrate host. One of the most commonly used PVD tools is Thermal evaporator. In this deposition tool, the bulk rock of the deposition material (source) is heated up to degrees in the order of 1000 C which turns the bulk rock into a melted liquid. This is happened by directing an extremely high current through the boat (the part of the system that source material is placed inside of it). Due to the existence of resistive heating in the boat material (which is generally a material with high melting temperature), the liquid material eventually starts to evaporate toward the target which is placed on top of the source. Typically, in a thermal evaporator tool, the source is located in the bottom of the chamber and the target is placed at the top. The distance between these two parts is about 1 m in our case to make sure that the evaporation beams approach the target with an almost uniform distribution. Specifically, in our case, in which the samples are as small as 1.5 cm x 1.5 cm, Tthe uniformity of the coating is quite well. Moreover, there is a rotating mechanism in the place of the sample holder to make sure that all parts of the sample experiences the same averaged evaporation rate. Fig. 14 shows the thermal evaporation system used in our depositions.

All of this process is made in high vacuum levels. When the chamber pressure happens to be very low, the amount of oxygen molecules inside the chamber becomes minimal. Therefore, the evaporation beam (particles) has minimum scattering due to minimized interaction leading to a long mean free path which is essentially in the order of couple of meters. To provide high vacuum levels

Figure 14. The utilized thermal evaporation system

system uses two different pumps; a mechanical pump, and a turbo pump. Mechanical pump is responsible for the first purging sections. In fact up to 10 mTorr chamber pressure, the mechanical pump is operating. Afterward, this pump is isolated from the system by a gate valve and higher vacuum levels are provided by a turbo pump. After evaporation started, the deposition rate (with a unit of A/s) starts to increase. This rate is recorded with an acoustic sensor monitor. Assuming that the source is acting as a point source that isotropically evaporate the source, we can formulate the deposition rate as:

$$\upsilon = \frac{R_{evp}}{4\pi N r^2} cos(\theta_i) \quad (4.1)$$

where R_{evp} is the evaporation rate of the source material in atoms of gram per second, N is the density of the source material, and r is the distance between the target and the source location. According to this formula, the deposition rate has cosine distribution in which the middle of the sample which is exactly located on top of the source would have the highest deposition rate and the corners have less deposition thicknesses at the end of the process. To avoid this, the distance of the source and sample is kept long enough to make the assumption of parallel rays valid. The deposition pressure is chosen as $\leq 6 \times 10^{-6}\, Torr$. The deposition of both Cr and Bi were made on a Tungsten (W) boat. The power was adjusted in a way that the deposition rate stays around 1 A/s. It should be mentioned that our experiences showed that higher deposition rates lead to a rough film surface and in the case of lower deposition rates the uniformity between the middle of the sample and the corners can lead to a hump profile where the middle part is thicker. The acoustic impedance and material density for Cr were written as 28.95, and 7.2 while these values for Bi is chosen as 11.18, and 9.8. After deposition of a 100 nm thick Cr layer, sample is taken into atomic layer deposition (ALD) chamber to deposit Al_2O_3 spacer layer.

4.1.3 Atomic Layer Deposition

Atomic layer deposition (ALD) is a tool from CVD family. In these deposition tool category, the atoms of the targeted material are chemically bonded into the surface of the substrate and therefore, they have stronger bonds compared to those of prepared with PVD systems. In ALD process, the source reactants are in the gas phase. The difference between the ALD and CVD deposition techniques is generally the deposition temperature. The required temperature for making the process happen is much lower in ALD case which opens up a door for making low temperature processes suitable for flexible electronics. Different from CVD method, in ALD the reactants do not exposed into the chamber simultaneously but they are sent by an order. The ALD process is made of successive cycles in which every cycle leads to the deposition of single atomic layer. Each deposition cycle (each of the two needed) are self-terminating where an angstrom thick layer is formed at the end of the process. As a

result, deposition rate is controllable to ˚A precision and the uniformity of the resulting films are superior. ALD is widely used in dielectric coating and recently, there are volatile precursors for metal coatings as well. In this system, there is no need for ultra-high vacuum. Moderate vacuum levels are enough to make the process happened. The utilized ALD system has been shown in the Fig. 15.

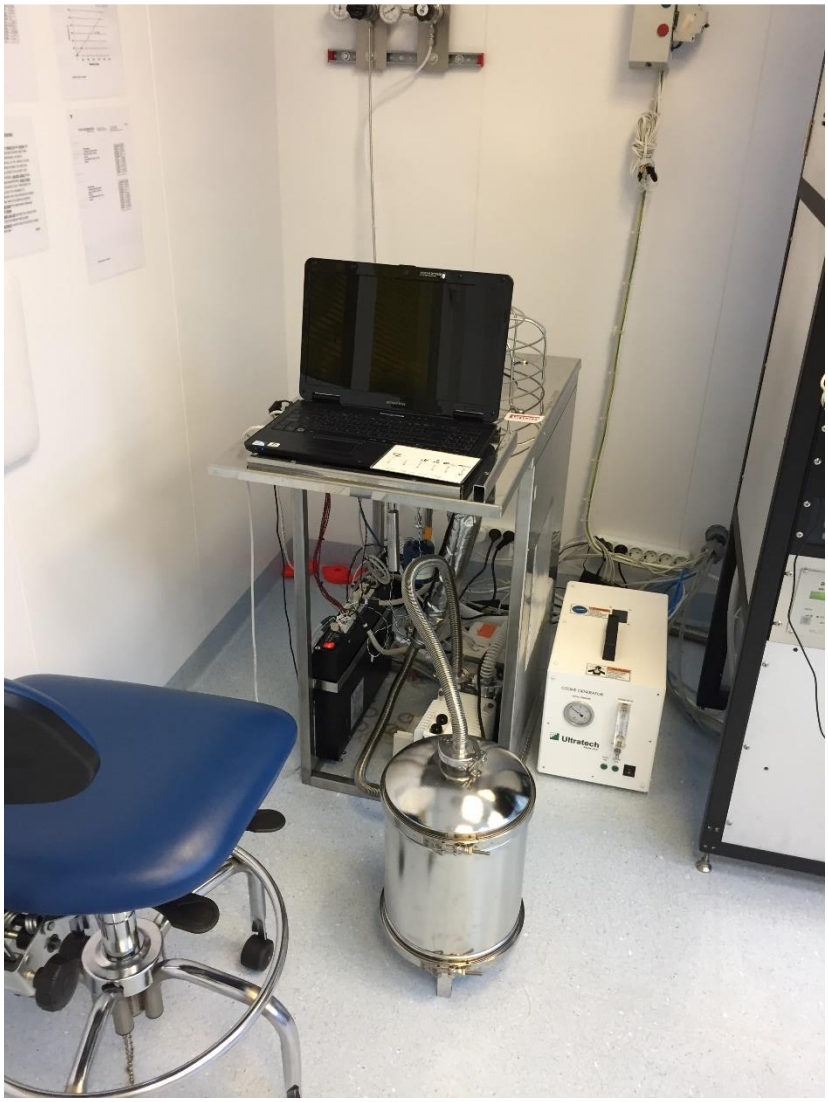

Figure 15. The utilized ALD system in deposition of Al_2O_3 layer.

4.1.3.1 ALD System Parts and Their Function

The ALD system comprises from the following parts:

***Carrier Gas*:** This carrier gas is N_2 which is an inert gas that does not react with any chemicals and only transport them toward the chamber. Also, when the process is

comleted, the bi-products are purged out using the same gas. A continuous flow of the inert gas is supplied in the system. The flow rate is adjusted for the device where the operating pressure is near 1 Torr.

Sources and precursors: The gaseous chemical source materials are put inside metallic cylinders. At the end of the bottle we have a microsecond valve that is opened in the time of pulsing and then, it is immediately closed. The minimum pulse time of this valve is 15 ms. The precursors for Al is Trimethyl aluminum (TMA) with a chemical formula of $Al(CH_3)_3$. The oxygen precursor is also DI water.

Heaters*:* Two planar and wire heaters have been connected into the chamber; one in the center of the chamber and the other is located in its circumference. By this way a uniform heat distribution is provided for the sample throughout the whole chamber. Moreover, two other heaters are wrapped around the pipelines to keep the gas temperature close the chamber temperature. Minimum required temperature to make the process happened is 80 C and increasing the temperature to higher values can increase the deposition rate. For very high temperatures, i.e. above 250 C, there might be the risk of precursor decomposition and unwanted reactions may take place. In our process, the temperature of chamber is fixed at 200 C while the line temperature is adjusted as 150 C.

***Reaction Chamber and Exhaust System*:** This is the place that reaction occurs and the film is formed on the sample. This chamber has one input and one output which gas goes inside and is purged out. A vacuum pump is responsible to purge the gas out and to keep the chamber in moderate pressure values.

4.1.3.2 The Operation Principle of ALD

As already told in previous sections, the ALD is a self-terminating process in which successive introduction of two different metal and oxygen contained gases will lead to formation of a monolayer of metal oxide layer. For this aim, carrier gas flow is adjusted as 20 sccm and a pulse time of 15 ms is adjusted for both Al and O precursors. After bringing the chamber temperature into a value of 200 C, first water is pulsed into the chamber and for 20 seconds the purge process is continued. Water is chemically adsorbed on the surface as OH groups.

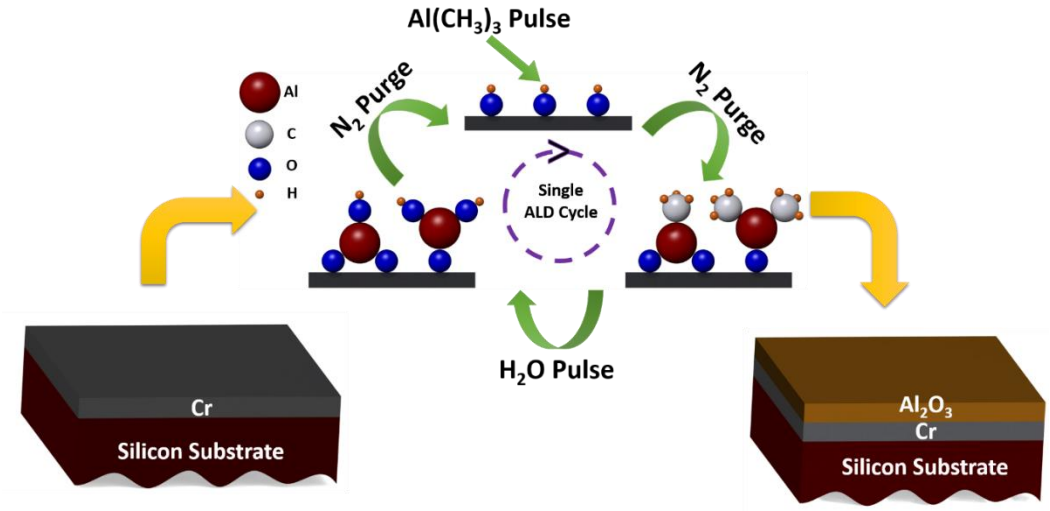

Figure 16. The schematic representation of ALD deposition of Al_2O_3 layer[102].

Then in the second half cycle, the TMA precursor is pulsed into the chamber with same pulse and purge times. In this half cycle the H molecule is de-attached from the surface and Al is chemically bonded into the surface. By this way, Al_2O_3 is formed. This has been schematically explained in Fig. 16. The chemical reaction of the process is as follows;

$$3H_2O + 2Al(CH_3)_3 \rightarrow Al_2O_3 + 6CH_4 \quad (4.2)$$

4.1.2 Electron Beam Lithography

To create the Nano patterns with dimensions much smaller than the wavelength, optical lithography is not a right choice. In this case, electron beam lithography (EBL) is utilized to create ultra-small precise nano-sized circular disk shaped patches. Because this technique uses electron beam rather than an optical wave, it can pattern the substrate with dimensions as small as tens of nanometers. To pattern nanodiscs on top of this sample, electron beam lithography (EBL, RAITH E-Line Plus) is used. For this purpose, 495 k PMMA resist with a thickness of 250 nm is spin-coated on the sample. The spin coating speed was set at 4000 rpm and the duration of this process is chosen as 60 seconds. The electron beam exposure was then performed with a beam writer at an acceleration voltage of 30 kV, e-beam spot size of 5 nm, and a 350 pA

beam current. A test dose study is conducted to find the proper values for realization of our desired dimensions. As the consequence of our optimizations, a single pixel dot exposure with a dose of 3000 pC is utilized for our final optimized sample. After the exposure, the samples are developed at room temperature by a MIBK:IPA (1:2) solution for 2 min followed by an immersion in IPA for 30 sec. At the last step, the Bi layer is coated on the sample by thermal evaporation and then lift off process is followed by placing sample in acetone solution for 4 hours.

4.2 Characterization

In this subsection, first a brief discussion on the operation mechanism of the fabrication facilities is provided for all the used equipment for the characterization of the fabricated structure and the measurement results will be presented. The characterization tools and methods will be presented in an order resembling the chronological order of their use throughout the design-fabrication-characterization cycle. Ellipsometry is utilized to optically characterize the permittivity data of each separate layer and to check its thickness. Scanning electron microscopy (SEM) was used to visualize the fabricated device and check the consistency of the device dimensions with the design. Finally, Fourier transform infrared spectroscopy (FTIR) spectroscopy is employed to obtain the absorption response of the overall MIM design.

4.2.1 Ellipsometry

An ellipsometer is a device, which is able to characterize the thickness and refractive index of a thin film sample. The device sends a polarized beam towards a sample on which the beam reflects. After the reflection, the reflected beam is measured in a polarization sensitive rotating analyzer. Thus the polarization change upon reflection can be monitored and the optical properties of the sample can be fit to a model. Fig. 17 shows the ellipsometry system that we used in our characterizations. The Bi metal used in the design were characterized before the actual device fabrication by ellipsometry. These material data were also used in the simulations. Fig. 18 shows the permittivity data for the Bi obtained using spectroscopic ellipsometry scans. For this aim, sample is put in the V-VASE ellipsometry equipment and the angled measurement is applied on the sample for five different incident angles of 55°, 60°,

65°, and 70°. Later the obtained data are fitted to extract the permittivity data of the blank Bi layer. As expected the real permittivity data stays below zero at lower wavelengths and goes to positive values as we move to longer wavelengths.

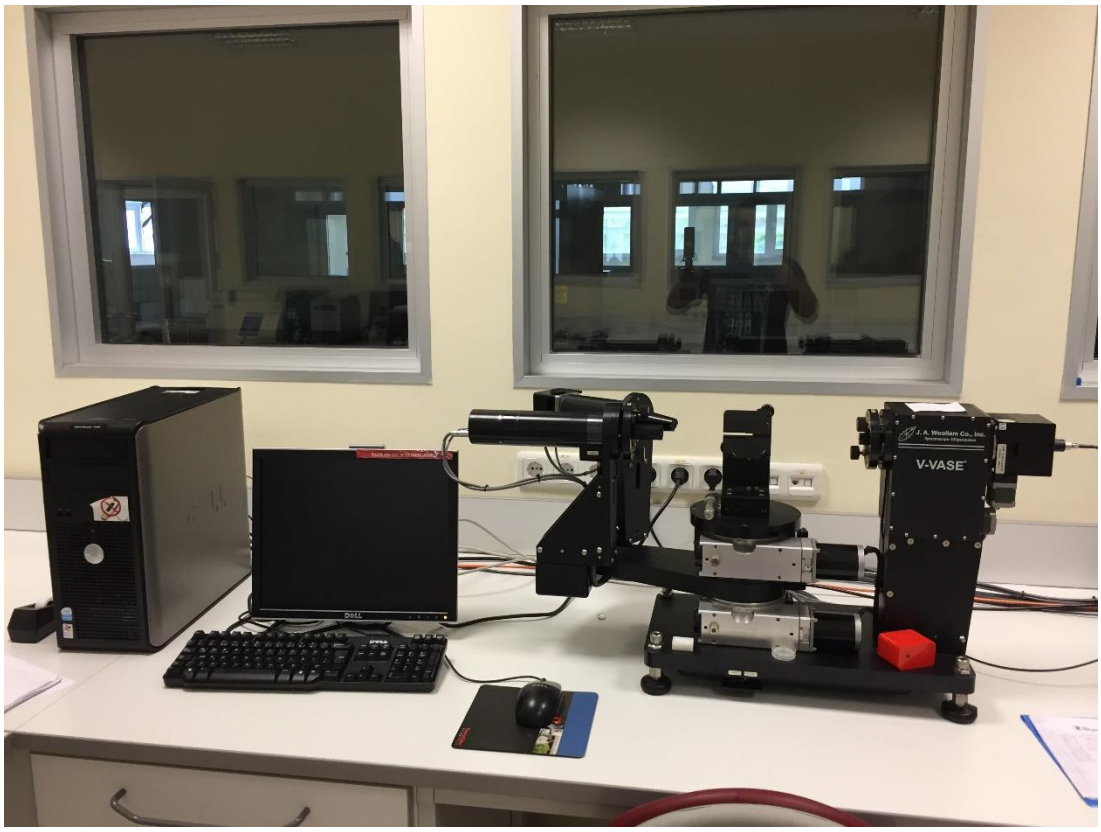

Figure 17. The ellipsometry system used in our characterizations.

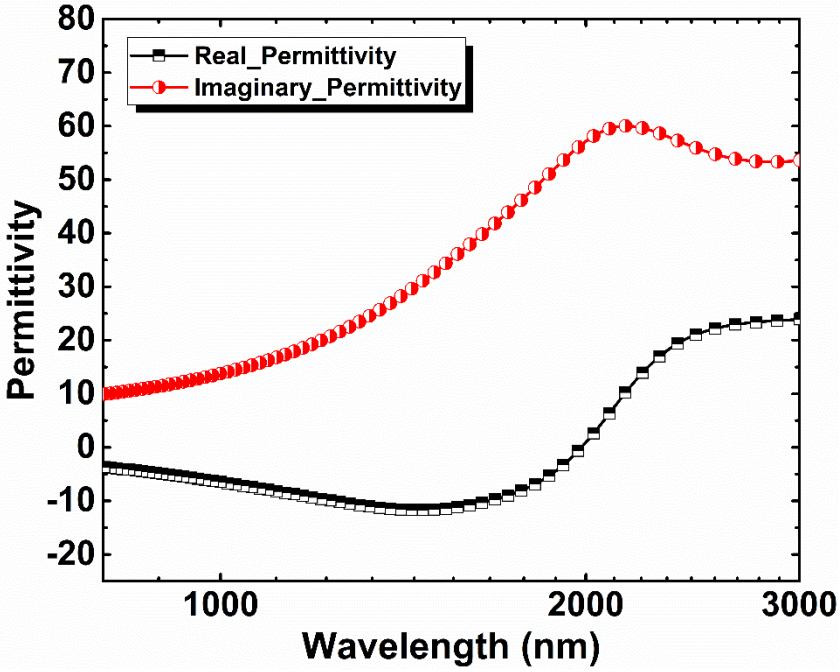

Figure 18. The extracted real and imaginary parts of permittivity for Bi metal layer.

Moreover, the thickness of the insulator layer deposited by the ALD was measured by the ellipsometer as well.

4.2.2 Scanning Electron Microscopy

As with any other electron microscopy method, scanning electron microscopy (SEM) uses accelerated electrons to image a sample. In an SEM setup, as shown in Fig. 19, an electron beam scans the surface while reflected (backscattered) and so called secondary electrons are simultaneously detected. This method requires the sample to be placed within a vacuum chamber before scanning is performed. This is required as the fragile electron source needs to be sustained in vacuum as well as collision of free electrons with gaseous molecules will render the method useless. Due to the low (De Broglie) wavelength of accelerated electrons compared with optical photons, the image resolution is relatively high. An SEM image can have up5 nm resolution. The method can become destructive for the sample if the intensity is increased. In our measurements, we checked the formation of nanodisc patterns on the sample using

Figure 19. SEM system used in our characterizations.

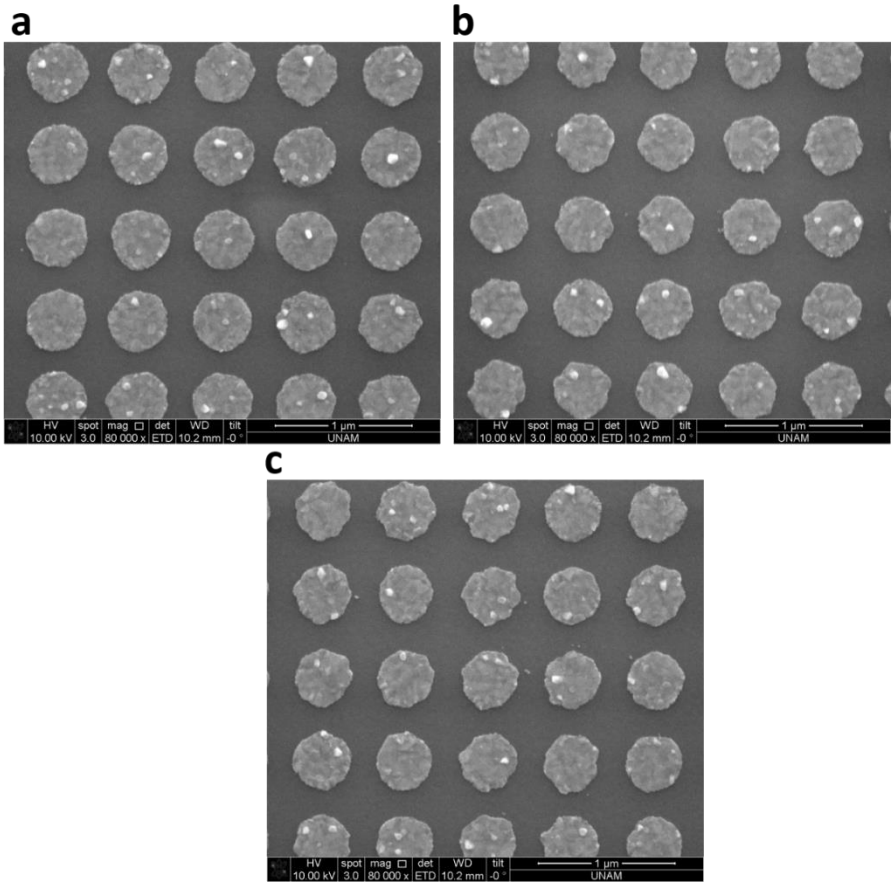

Figure 20. The top view SEM images of different nanodisc radius sizes of (a) 220 nm, (b) 210 nm, and (c) 200 nm.

top view SEM image. As shown in Fig. 20, three different disc radii of 220 nm, 210 nm, and 200 nm were made by adjusting the exposure intensity of the beam.

4.2.3 Fourier Transform Infrared Spectroscopy

Although there are different methods to optically characterize the absorption response of a design, in this study, we only used the reflective FTIR characterization. The FTIR technique is an indirect, interferometric measurement technique, able to acquire a broad spectral response in the near infrared (NIR) and far infrared (FIR) regimes in a relatively short time. The power comes from the ability of the setup to collect all wavelengths simultaneously. Interferogram of the signal is obtained through an interferometer and a Fourier transform is performed on the interferogram to finally obtain the spectrum. An FTIR setup digitally collects the intefreogram data and computes the Fourier transform. As its name suggests, the method works well in the infrared regime and the significantly advantageous due to the high signal to noise ratio achievable with high spectral resolution and accuracy. The system is shown in Fig. 21.

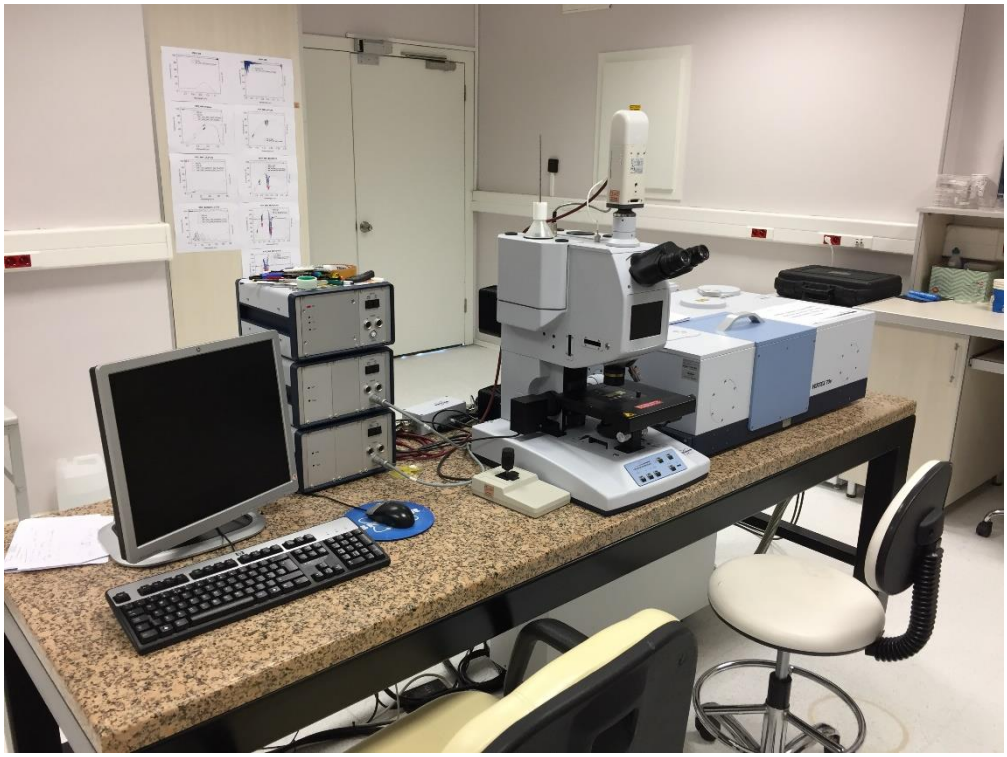

Figure 21. The FTIR system

Finally, to experimentally verify our simulation findings, the optimized design has been fabricated and optically characterized using Fourier-transform infrared spectroscopy (FTIR) equipment. For this aim, three different radii of R = 200 nm, 210 nm, and 220 nm have been fabricated by choosing proper exposure doses. Ellipsometry measurements have been conducted on a test Al_2O_3 coated Si sample to find the thickness of the spacer layer. The measurement shows that the thickness of the layer is 143 nm which is quite close to our target thickness of 145 nm. Also stylus profilometer measurement revealed that the thickness of top nanodiscs is 24 nm which is again close to our target. As shown in Fig. 11, the increase in the radius of nanodiscs induces a slight red shift in the position of the second mode which is in line with our numerical findings. According to these measurement results, an absorption above 0.9 has been obtained in an ultra-broadband range of 800 nm- 2410 nm which is the broadest reported MIM absorber, to the best of our knowledge. This has been shown in Fig. 22. The average absorption is also calculated using above equation and it is found to be 0.92 in the range covering from 800 nm to 3000 nm.

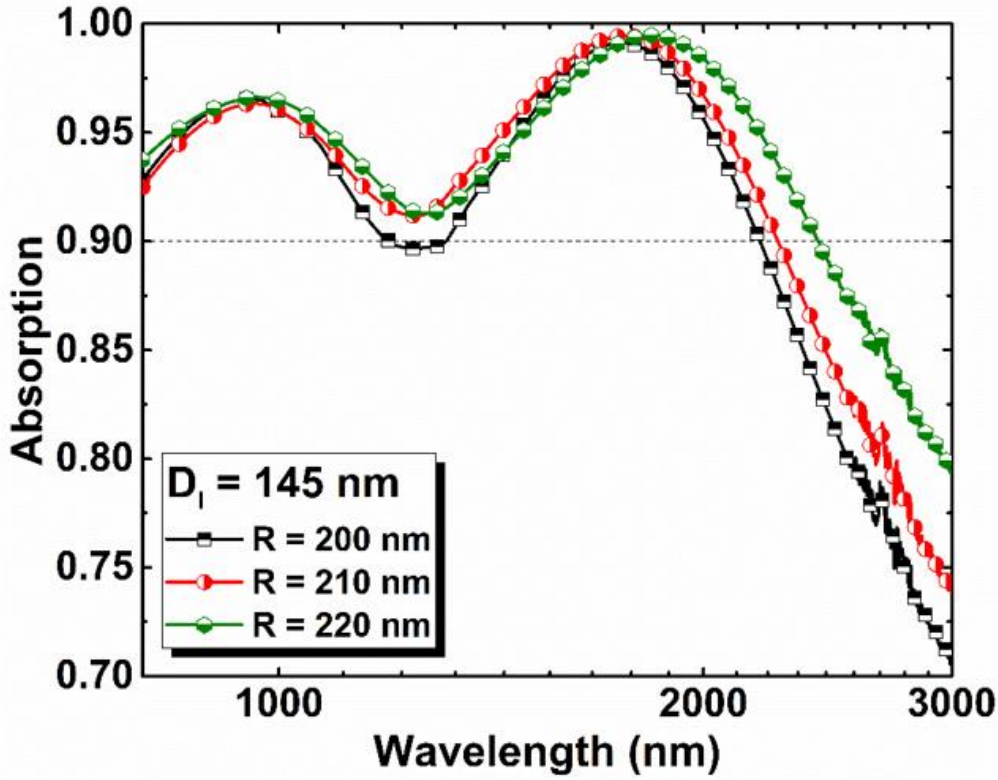

Figure 22. The measured absorption spectra of the MIM design with three different disc radii.

CHAPTER 5

CONCLUSION AND FUTURE DIRECTION

This thesis was concerned with the design and experimental demonstration of a broadband metamaterial absorber. The subject can be classified as a 'hot' topic at least around the time this thesis was written. The results in terms of the relative bandwidth obtained in this thesis are record breaking. Upper absorption edge to lower absorption edge ratio is used a measure of relative bandwidth in current literature. For the designed and fabricated device, this ratio was demonstrated to be 3:1, which spans more than an octave. Moreover, the upper absorption edge wavelength corresponds to approximately 10 times the total thickness of the absorber. Therefore the structure absorbs a broadband electromagnetic radiation within a thickness much shorter than the operation wavelength. This project was carried out through design, simulation, fabrication and characterization cycle which is used commonly within the scientific community. The design and simulation was performed using a commercial software Lumerical FDTD Solutions. The software also accepts n-k data of materials obtained from optical measurements. This was a crucial step before the final and successful design was simulated and consequently led to successful expermental results. Development involved many simulations and a parameter optimization study before the design was completed. An iterative approach was used and the optimization was carried out for four parameters: insulator thickness, top layer metal thickness, top layer disk radius and pitch (or periodicity). The optimal design was not only aimed to have the broadest absorption bandwidth but also small sensitivity to fabrication errors.

The fabrication steps were thermal evaporation, ALD and EBL. Thermal evaporation step was used for the evaporation of firstly of Cr. This step was followed by ALD of alumina. The sample was covered with pmma and patterned with EBL before Bi was

evaporated on the top layer. After Bi was evaporated on the patterned pmma, lift-off was performed and the final device was obtained.

The characterization tools used were ellipsometer, SEM and FTIR. Ellipsometer was an important tool for the absorber design both before and during the fabrication cycle. The material data generated by the ellipsometer was used in the simulations also the thickness of the insulator layer (alumina) was measured by this device. After the fabrication was complete, SEM tool was used to generate images of the device and measure the dimensions of the Bi nanodisks on the top layer. The device was finally characterized by FTIR and the absorption spectrum obtained in this step was the conclusion of experimental efforts of this project. The results obtained in this thesis show that material selection and optimization are crucial in the design of broadband metamaterial absorbers and can lead to record breaking results.

As their name implies, an ultra broadband metamaterial absorber design is as good as its absorption bandwidth. As the bandwidth broadens, the device gets more functional for the desired applications such as solar light harvesting. Therefore the main aim is to further broaden the bandwidth. For this aim the are some ideas present and they will be presented here. First idea is to use multiple patterns on the top layer. The simples idea is to use two different radii for the nanodisk layer. In such a structure, different resonances are introduced due to different radii of the disks. This ability to introduce different resonances will give us another degree of freedom in the design and clearly pave the way for a broader bandwidth. In such a scheme, the number of parameters to be optimized will be 5 instead of 4. The approach used throughout this project can be similarly applied. There might be drawbacks of such a structure however. The increased unit cell size implies a reduced symmetry (group) which might slightly affect omnidirectionality and polarization insensitivity. To shortly elaborate on this, it can be said that with two different radii, the unit cell will be composed of 4 disks (2 big 2 small) and therefore the structure will be less-periodic. Also some of the rotational and reflection (mirror) symmetries will disappear when the transition from single radius structure to a two radii structure occurs. This will have consequences on the polarization insensitivity to some degree as the rotated structure will not be identical to the structure before rotation. The degree of polarization insensitivity

degradation should be investigated. Another structure to investigate is the hexagonal (or triangular) periodic lattice. This structure is more symmetric than the rectangular lattice and is expected to have a better polarization insensitivity. This structure is however more difficult to simulate as FDTD method relies on rectangular simulation domain and a hexagonal lattice can be implemented in rectangular simulation domain with a bigger unit cell.

REFERRENCES

[1] D. Jariwala, A. R. Davoyan, J. Wong, and H. A. Atwater, "Van der Waals Materials for Atomically-Thin Photovoltaics: Promise and Outlook," *ACS Photonics*, vol. 4, pp. 2962–2970, 2017.

[2] Palik, "E. D. Handbook of optical constants of solids. Vol. 3 (Academic press, 1998)."

[3] D. R. Smith, J. B. Pendry, and M. C. K. Wiltshire, "Metamaterials and Negative Refractive Index," *Science (80-.).*, vol. 305, pp. 788–793, 2004.

[4] J. Yao *et al.*, "Optical Negative Refraction in Bulk Metamaterials of Nanowires," *Science (80-.).*, vol. 321, p. 930, 2008.

[5] A. J. Hoffman *et al.*, "Negative refraction in semiconductor metamaterials," *Nat. Mater.*, vol. 6, pp. 946–950, 2007.

[6] M. Lapine, I. V Shadrivov, D. A. Powell, and Y. S. Kivshar, "Magnetoelastic metamaterials," *Nat. Mater.*, vol. 11, no. 1, pp. 30–33, 2011.

[7] D. Fleischman, A. Davoyan, P. Yeh, and H. A. Atwater, "Optical magnetism in planar metamaterial heterostructures," *Nat. Commun.*, vol. 9, p. 296, 2018.

[8] C. Menzel *et al.*, "Asymmetric transmission of linearly polarized light at optical metamaterials," *Phys. Rev. Lett.*, vol. 104, no. 25, p. 253902, 2010.

[9] Z. Li, M. Mutlu, and E. Ozbay, "Chiral metamaterials : from optical activity and negative refractive index to asymmetric transmission," *J. Opt.*, vol. 15, p. 023001, 2013.

[10] A. Fang, T. Koschny, and C. M. Soukoulis, "Lasing in metamaterial nanostructures," *J. Opt.*, vol. 12, p. 024013, 2010.

[11] E. Plum, V. A. Fedotov, P. Kuo, D. P. Tsai, and N. I. Zheludev, "Towards the lasing spaser : controlling metamaterial optical response with semiconductor quantum dots," *Opt. Express*, vol. 17, no. 10, pp. 11–14, 2009.

[12] D. Schurig *et al.*, "Metamaterial Electromagnetic Cloak at Microwave Frequencies," *Science (80-.).*, vol. 314, pp. 977–981, 2006.

[13] J. Valentine, J. Li, T. Zentgraf, G. Bartal, and X. Zhang, "An optical cloak made of dielectrics," *Nat. Mater.*, vol. 8, no. 7, pp. 568–571, 2009.

[14] T. Ergin, N. Stenger, P. Brenner, J. B. Pendry, and M. Wegener, "Three-dimensional invisibility cloak at optical wavelengths," *Science (80-.).*, vol. 328, no. 5976, pp. 337–339, 2010.

[15] N. I. Landy, S. Sajuyigbe, J. J. Mock, D. R. Smith, and W. J. Padilla, “Perfect Metamaterial Absorber,” *Phys. Rev. Lett.*, vol. 100, p. 207402, 2008.

[16] M. E. Stewart *et al.*, “Nanostructured Plasmonic Sensors,” *Chem. Rev.*, vol. 108, pp. 494–521, 2008.

[17] P. Offermans, M. C. Schaafsma, S. R. K. Rodriguez, Y. Zhang, and M. Crego-calama, “Universal Scaling of the Figure of Merit of Plasmonic Sensors,” *ACS Nano*, vol. 5, no. 6, pp. 5151–5157, 2011.

[18] T. Xu, Y.-K. Wu, X. Luo, and L. J. Guo, “Plasmonic nanoresonators for high-resolution colour filtering and spectral imaging,” *Nat. Commun.*, vol. 1, p. 59, 2010.

[19] N. I. Landy, C. M. Bingham, T. Tyler, N. Jokerst, D. R. Smith, and W. J. Padilla, “Design, theory, and measurement of a polarization-insensitive absorber for terahertz imaging,” *Phys. Rev. B - Condens. Matter Mater. Phys.*, vol. 79, no. 12, pp. 1–6, 2009.

[20] A. Tittl *et al.*, “A Switchable Mid-Infrared Plasmonic Perfect Absorber with Multispectral Thermal Imaging Capability,” *Adv. Mater.*, vol. 27, pp. 4597–4603, 2015.

[21] T. Ellenbogen, K. Seo, and K. B. Crozier, “Chromatic Plasmonic Polarizers for Active Visible Color Filtering and Polarimetry,” *Nano Lett.*, vol. 12, pp. 1026–1031, 2012.

[22] S. Yokogawa, S. P. Burgos, and H. A. Atwater, “Plasmonic color filters for CMOS image sensor applications,” *Nano Lett.*, vol. 12, no. 8, pp. 4349–4354, 2012.

[23] C. Ji, K. T. Lee, T. Xu, J. Zhou, H. J. Park, and L. J. Guo, “Engineering Light at the Nanoscale: Structural Color Filters and Broadband Perfect Absorbers,” *Adv. Opt. Mater.*, vol. 5, no. 20, p. 1700368, 2017.

[24] T. G. Ulusoy Ghobadi, A. Ghobadi, T. Okyay, K. Topalli, and A. K. Okyay, “Controlling luminescent silicon nanoparticle emission produced by nanosecond pulsed laser ablation: role of interface defect states and crystallinity phase,” *RSC Adv.*, vol. 6, no. 113, 2016.

[25] E. Rephaeli and S. Fan, “Absorber and emitter for solar thermo-photovoltaic systems to achieve efficiency exceeding the Shockley-Queisser limit,” *Opt. Express*, vol. 17, no. 17, pp. 15145–15159, 2009.

[26] J. K. Tong, W. Hsu, Y. Huang, S. V Boriskina, and G. Chen, “Thin-film ‘ Thermal Well ’ Emitters and Absorbers for High-Efficiency Thermophotovoltaics,” *Sci. Rep.*, vol. 5, p. 10661, 2015.

[27] C. Wu *et al.*, “Metamaterial-based integrated plasmonic absorber / emitter for solar thermo-photovoltaic systems,” *J. Opt.*, vol. 14, p. 024005, 2012.

[28] T. I. A. N. J. I. L. Iu and J. U. T. Akahara, “Ultrabroadband absorber based on single- sized embedded metal-dielectric-metal structures and application of

radiative cooling," *Opt. Express*, vol. 25, no. 12, pp. 1443–1447, 2017.

[29] D. Wu *et al.*, "The design of ultra-broadband selective near-perfect absorber based on photonic structures to achieve near-ideal daytime radiative cooling," *Mater. Des.*, vol. 139, pp. 104–111, 2018.

[30] E. Rephaeli, A. Raman, and S. Fan, "Ultrabroadband Photonic Structures To Achieve High-Performance Daytime Radiative Cooling," *Nano Lett.*, vol. 13, pp. 1457–1461, 2013.

[31] F. P. G. de Arquer, A. Mihi, and G. Konstantatos, "Large-Area Plasmonic-Crystal−Hot-Electron-Based Photodetectors," *ACS Photonics*, vol. 2, pp. 950–957, 2015.

[32] W. Li and J. Valentine, "Metamaterial Perfect Absorber Based Hot Electron Photodetection," *Nano Lett.*, vol. 14, pp. 3510–3514, 2014.

[33] T. G. U. Ghobadi, A. Ghobadi, E. Ozbay, and F. Karadas, "Strategies for Plasmonic Hot-Electron-Driven Photoelectrochemical Water Splitting," *ChemPhotoChem*, vol. 2, pp. 1–23, 2018.

[34] J. Fang *et al.*, "Ag/diatomite for highly efficient solar vapor generation under one-sun irradiation," *J. Mater. Chem. A*, vol. 5, pp. 17817–17821, 2017.

[35] K. Bae, G. Kang, S. K. Cho, W. Park, W. J. Padilla, and K. Kim, "Flexible thin-film black gold membranes with ultrabroadband plasmonic nanofocusing for efficient solar vapour generation," *Nat. Commun.*, vol. 6, pp. 1–9, 2015.

[36] L. Zhou *et al.*, "Self-assembly of highly efficient, broadband plasmonic absorbers for solar steam generation," *Sci. Adv.*, vol. 2, no. 4, pp. e1501227–e1501227, 2016.

[37] J. Park *et al.*, "Omnidirectional Near-Unity Absorption in an Ultrathin Planar Semiconductor Layer on a Metal Substrate," *ACS Photonics*, vol. 1, pp. 812–821, 2014.

[38] C. Hägglund and S. P. Apell, "Plasmonic Near-Field Absorbers for Ultrathin Solar Cells," *Phys. Chem. Lett.*, vol. 3, pp. 1275–1285, 2012.

[39] P. Detectors, M. Entezari, and M. Zavvari, "Application of Hyperbolic Metamaterials for Responsivity Enhancement of Thin Film Photo-Conductive Detectors," *IEEE Sens. J.*, vol. 16, no. 24, pp. 8916–8920, 2016.

[40] W. Wang, A. Klots, D. Prasai, Y. Yang, K. I. Bolotin, and J. Valentine, "Hot Electron-Based Near-Infrared Photodetection Using Bilayer MoS 2," *Nano Lett.*, vol. 15, pp. 7440–7444, 2015.

[41] A. Ghobadi, H. I. Yavuz, T. G. Ulusoy, K. C. Icli, M. Ozenbas, and A. K. Okyay, "Electrochimica Acta Enhanced Performance of Nanowire-Based All-TiO 2 Solar Cells using Subnanometer-Thick Atomic Layer Deposited ZnO Embedded Layer," *Electrochim. Acta*, vol. 157, pp. 23–30, 2015.

[42] V. E. Ferry *et al.*, "Light trapping in ultrathin plasmonic solar cells," *Opt.*

Express, vol. 18, pp. 237–245, 2010.

[43] O. Lopez-Sanchez, E. Alarcon Llado, V. Koman, A. Fontcuberta I Morral, A. Radenovic, and A. Kis, "Light generation and harvesting in a van der waals heterostructure," *ACS Nano*, vol. 8, no. 3, pp. 3042–3048, 2014.

[44] P. Spinelli *et al.*, "Plasmonic light trapping in thin-film Si solar cells," *J. Opt.*, vol. 14, p. 024002, 2012.

[45] Y. Wang, T. Sun, T. Paudel, Y. Zhang, Z. Ren, and K. Kempa, "Metamaterial-Plasmonic Absorber Structure for High Efficiency Amorphous Silicon Solar Cells," *Nano Lett.*, vol. 12, pp. 440–445, 2012.

[46] M. A. Green and S. Pillai, "Harnessing plasmonics for solar cells," *Nat. Photonics*, vol. 6, pp. 130–132, 2012.

[47] N. Vandamme, N. Bardou, and C. Dupuis, "Metal Nanogrid for Broadband Multiresonant Light-Harvesting in Ultrathin GaAs Layers," *ACS Photonics*, vol. 1, pp. 878–884, 2014.

[48] C. F. Guo, T. Sun, F. Cao, Q. Liu, and Z. Ren, "Metallic nanostructures for light trapping in energy-harvesting devices," *Light Sci. Appl.*, vol. 42, pp. 1–12, 2014.

[49] A. Ahmadivand, M. Karabiyik, and N. Pala, *6. Plasmonic photodetectors*. Elsevier Ltd, 2016.

[50] S. Ogawa and M. Kimata, "Metal-Insulator-Metal-Based Plasmonic Metamaterial Absorbers at Visible and Infrared Wavelengths: A Review," *Materials (Basel).*, vol. 11, no. 458, pp. 1–18, 2018.

[51] N. Liu, M. Mesch, T. Weiss, M. Hentschel, and H. Giessen, "Infrared perfect absorber and its application as plasmonic sensor," *Nano Lett.*, vol. 10, no. 7, pp. 2342–2348, 2010.

[52] K. Aydin, V. E. Ferry, R. M. Briggs, and H. a. Atwater, "Broadband polarization-independent resonant light absorption using ultrathin plasmonic super absorbers," *Nat. Commun.*, vol. 2, p. 517, 2011.

[53] J. Hao, J. Wang, X. Liu, W. J. Padilla, L. Zhou, and M. Qiu, "High performance optical absorber based on a plasmonic metamaterial," *Appl. Phys. Lett.*, vol. 96, p. 251104, 2010.

[54] M. K. Hedayati *et al.*, "Design of a perfect black absorber at visible frequencies using plasmonic metamaterials," *Adv. Mater.*, vol. 23, no. 45, pp. 5410–5414, 2011.

[55] J. Hao, L. Zhou, and M. Qiu, "Nearly total absorption of light and heat generation by plasmonic metamaterials," *Phys. Rev. B*, vol. 83, p. 165107, 2011.

[56] C. M. Watts, X. Liu, and W. J. Padilla, "Metamaterial Electromagnetic Wave Absorbers," *Adv. Opt. Mater.*, vol. 24, pp. OP98–OP120, 2012.

[57] A. Ghobadi *et al.*, “Visible light nearly perfect absorber: an optimum unit cell arrangement for near absolute polarization insensitivity,” *Opt. Express*, vol. 25, no. 22, p. 27624, 2017.

[58] A. Ghobadi, H. Hajian, A. R. Rashed, B. Butun, and E. Ozbay, “Tuning the metal filling fraction in absorbers to maximize the absorption bandwidth,” *Photonics Reseach*, vol. 6, no. 3, pp. 168–176, 2018.

[59] Q. Wen, Y. Xie, H. Zhang, Q. Yang, and Y. Li, “Transmission line model and fields analysis of metamaterial absorber in the terahertz band,” *Opt. Express*, vol. 17, no. 22, pp. 20256–20265, 2009.

[60] M. Yan, “Metal-insulator-metal light absorber: a continuous structure,” *J. Opt.*, vol. 15, no. 2, p. 25006(1-8), 2013.

[61] H. Tao *et al.*, “A dual band terahertz metamaterial absorber,” *J. Phys. D. Appl. Phys.*, vol. 43, p. 225102, 2010.

[62] Z. Yong, S. Zhang, C. Gong, and S. He, “Narrow band perfect absorber for maximum localized magnetic and electric field enhancement and sensing applications,” *Sci. Rep.*, vol. 6, p. 24063, 2016.

[63] P. Mandal, “plasmonic metamaterial perfect absorber at visible frequency : design rule,” *J. Nanophotonics*, vol. 11, no. 3, p. 036003, 2017.

[64] B. Wang, W.-Q. Huang, and L.-L. Wang, “Ultra-narrow terahertz perfect light absorber based on surface lattice resonance of a sandwich resonator for sensing applications,” *RSC Adv.*, vol. 7, pp. 42956–42963, 2017.

[65] D. Wu *et al.*, “Infrared Perfect Ultra-narrow Band Absorber as Plasmonic Sensor,” *Nanoscale Res. Lett.*, vol. 11, no. 1, p. 483, 2016.

[66] J. Kim, K. Han, and J. W. Hahn, “Selective dual-band metamaterial perfect absorber for infrared stealth technology,” *Sci. Rep.*, vol. 7, p. 6740, 2017.

[67] S. Shu, Z. Li, and Y. Y. Li, “Triple-layer Fabry-Perot absorber with near-perfect absorption in visible and near-infrared regime,” *Opt. Express*, vol. 21, no. 21, pp. 4795–4801, 2013.

[68] Y. S. Do and K. C. Choi, “Poly-periodic hole arrays for angle-invariant plasmonic filters,” *Opt. Lett.*, vol. 40, no. 16, pp. 3873–3876, 2015.

[69] A. Moreau *et al.*, “Controlled-reflectance surfaces with film-coupled colloidal nanoantennas,” *Nature*, vol. 492, pp. 86–90, 2012.

[70] A. Cattoni, P. Ghenuche, D. Decanini, J. Chen, and J. Pelouard, “λ3/1000 Plasmonic Nanocavities for Biosensing Fabricated by Soft UV Nanoimprint Lithography,” *Nano Lett.*, vol. 11, pp. 3557–3563, 2011.

[71] N. Zhang *et al.*, “Reversibly tunable coupled and decoupled super absorbing structures,” *Appl. Phys. Lett.*, vol. 108, p. 091105, 2016.

[72] W. Chang, J. Won, L. S. Slaughter, and S. Link, “Plasmonic nanorod absorbers as orientation sensors,” *PNAS*, vol. 107, no. 7, pp. 2781–2786, 2010.

[73] Y. Avitzour, Y. A. Urzhumov, and G. Shvets, “Wide-angle infrared absorber based on a negative-index plasmonic metamaterial,” *Phys. Rev. B*, vol. 79, no. 4, pp. 1–5, 2009.

[74] X. Liu, T. Starr, A. F. Starr, and W. J. Padilla, “Infrared Spatial and Frequency Selective Metamaterial with Near-Unity Absorbance,” *Phys. Rev. Lett.*, vol. 104, p. 207403, 2010.

[75] H. Wang and L. Wang, “Perfect selective metamaterial solar absorbers,” *Opt. Express*, vol. 21, no. S6, pp. 13311–13319, 2013.

[76] M. G. Nielsen, A. Pors, O. Albrektsen, and S. I. Bozhevolnyi, “Efficient absorption of visible radiation by gap plasmon resonators,” *Opt. Express*, vol. 20, no. 12, pp. 13311–13319, 2012.

[77] X. Ming and Q. Tan, “Design Method of a Broadband Wide-Angle Plasmonic Absorber in the Visible Range,” *Plasmonics*, vol. 12, no. 1, pp. 14–17, 2017.

[78] M. Kenney, J. Grant, Y. D. Shah, I. Escorcia-carranza, M. Humphreys, and D. R. S. Cumming, “Octave-Spanning Broadband Absorption of Terahertz Light Using Metasurface Fractal-Cross Absorbers,” *ACS Photonics*, vol. 4, pp. 2604–2612, 2017.

[79] X. Duan, S. Chen, W. Liu, H. Cheng, and Z. Li, “Polarization-insensitive and wide-angle broadband nearly perfect absorber by tunable planar metamaterials in the visible regime,” *J. Opt.*, vol. 16, p. 125107, 2014.

[80] A. K. Azad *et al.*, “Metasurface Broadband Solar Absorber,” *Sci. Rep.*, vol. 6, p. 20347, 2016.

[81] R. Mudachathi and T. Tanaka, “Broadband plasmonic perfect light absorber in the visible spectrum for solar cell applications,” *Adv. Nat. Sci. Nanosci. Nanotechnol.*, vol. 9, p. 015010, 2018.

[82] C. S. Park, V. R. Shrestha, S. S. Lee, and D. Y. Choi, “Trans-Reflective Color Filters Based on a Phase Compensated Etalon Enabling Adjustable Color Saturation,” *Sci. Rep.*, vol. 6, p. 25496, 2016.

[83] Z. Li, S. Butun, and K. Aydin, “Large-area, Lithography-free super absorbers and color filters at visible frequencies using ultrathin metallic films,” *ACS Photonics*, vol. 2, no. 2, pp. 183–188, 2015.

[84] Y. Zhao *et al.*, “Artificial structural color pixels: A review,” *Materials (Basel).*, vol. 10, p. 944, 2017.

[85] Y.-T. Yoon and S.-S. Lee, “Transmission type color filter incorporating a silver film based etalon.,” *Opt. Express*, vol. 18, no. 5, pp. 5344–5349, 2010.

[86] D. Zhao *et al.*, “Ultra-narrow-band light dissipation by a stack of lamellar silver and alumina,” *Appl. Phys. Lett.*, vol. 104, p. 221107, 2014.

[87] J. Y. Lee, K. T. Lee, S. Seo, and L. J. Guo, “Decorative power generating panels creating angle insensitive transmissive colors,” *Sci. Rep.*, vol. 4, p. 4192, 2014.

[88] S. S. Mirshafieyan and D. A. Gregory, “Electrically tunable perfect light absorbers as color filters and modulators,” *Sci. Rep.*, no. January, pp. 1–9, 2018.

[89] H. A. O. P. Eng, Y. I. L. Uo, X. I. Y. Ing, Y. P. U. Ang, Y. A. J. Iang, and J. X. U. Immy, “Broadband and highly absorbing multilayer structure in mid-infrared,” *Appl. Opt.*, vol. 55, no. 31, pp. 8833–8838, 2016.

[90] Z. Li, E. Palacios, S. Butun, H. Kocer, and K. Aydin, “Omnidirectional, broadband light absorption using large-area, ultrathin lossy metallic film coatings,” *Sci. Rep.*, vol. 5, p. 15137, 2015.

[91] A. Ghobadi, S. A. Dereshgi, B. Butun, and E. Ozbay, “Ultra-broadband Asymmetric Light Transmission and Absorption Through The Use of Metal Free Multilayer Capped Dielectric Microsphere Resonator,” *Sci. Rep.*, vol. 7, p. 14538, 2017.

[92] N. Mattiucci, M. J. Bloemer, N. Akozbek, and G. D’Aguanno, “Impedance matched thin metamaterials make metals absorbing,” *Sci. Rep.*, vol. 3, no. 3203, pp. 1–11, 2013.

[93] M. Chirumamilla *et al.*, “Multilayer tungsten-alumina-based broadband light absorbers for high-temperature applications,” *Opt. Mater. Express*, vol. 6, no. 8, p. 2704, 2016.

[94] K. Mao *et al.*, “Angle insensitive color filters in transmission covering the visible region,” *Sci. Rep.*, vol. 6, p. 19289, 2016.

[95] H. Deng, Z. Li, L. Stan, D. Rosenmann, and D. Czaplewski, “Broadband perfect absorber based on one ultrathin layer of refractory metal,” *Opt. Lett.*, vol. 40, no. 11, pp. 2592–2595, 2015.

[96] G. Kajtár, M. Kafesaki, E. N. Economou, and C. M. Soukoulis, “Theoretical model of homogeneous metal–insulator–metal perfect multi-band absorbers for the visible spectrum,” *J. Phys. D. Appl. Phys.*, vol. 49, no. 5, p. 055104, 2016.

[97] F. Ding *et al.*, “Lithography-free, broadband, omnidirectional, and polarization-insensitive thin optical absorber,” *Appl. Phys. Lett.*, vol. 106, p. 061108, 2015.

[98] Y. K. Zhong *et al.*, “Omnidirectional, polarization-independent, ultra-broadband metamaterial perfect absorber using field-penetration and reflected-wave-cancellation,” *Opt. Express*, vol. 24, no. 10, p. A832, 2016.

[99] Y. K. Zhong *et al.*, “Fully Planarized Perfect Metamaterial Absorbers With No Photonic Nanostructures,” *IEEE Photonics J.*, vol. 8, no. 1, p. 2200109, 2016.

[100] S. M. Fu, Y. K. Zhong, M. H. Tu, B. R. Chen, and A. Lin, “A fully functionalized metamaterial perfect absorber with simple design and implementation,” *Sci. Rep.*, vol. 6, p. 36244, 2016.

[101] A. Ghobadi, S. A. Dereshgi, H. Hajian, B. Bozok, B. Butun, and E. Ozbay, “Ultra-broadband , wide angle absorber utilizing metal insulator multilayers stack with a multi- thickness metal surface texture,” *Sci. Rep.*, vol. 7, p. 4755, 2017.

[102] A. Ghobadi, H. Hajian, S. A. Dereshgi, B. Bozok, B. Butun, and E. Ozbay, "Disordered Nanohole Patterns in Metal-Insulator Multilayer for Ultra-broadband Light Absorption: Atomic Layer Deposition for Lithography Free Highly repeatable Large Scale Multilayer Growth," *Sci. Rep.*, vol. 7, p. 15079, 2017.

[103] S. Abedini Dereshgi, A. Ghobadi, H. Hajian, B. Butun, and E. Ozbay, "Ultra-Broadband, Lithography-Free, and Large-Scale Compatible Perfect Absorbers: The Optimum Choice of Metal layers in Metal-Insulator Multilayer Stacks," *Sci. Rep.*, vol. 7, no. 1, 2017.

[104] C. S. Park, V. R. Shrestha, S. S. Lee, E. S. Kim, and D. Y. Choi, "Omnidirectional color filters capitalizing on a nano-resonator of Ag-TiO2 -Ag integrated with a phase compensating dielectric overlay," *Sci. Rep.*, vol. 5, p. 8467, 2015.

[105] K.-T. Lee, S. Seo, J. Y. Lee, and L. J. Guo, "Strong resonance effect in a lossy medium-based optical cavity for angle robust spectrum filters.," *Adv. Mater.*, vol. 26, no. 36, pp. 6324–6328, 2014.

[106] J. H. Han, D.-Y. Kim, D. Kim, and K. C. Choi, "Highly conductive and flexible color filter electrode using multilayer film structure," *Sci. Rep.*, vol. 6, p. 29341, 2016.

[107] K. T. Lee, S. Seo, J. Yong Lee, and L. Jay Guo, "Ultrathin metal-semiconductor-metal resonator for angle invariant visible band transmission filters," *Appl. Phys. Lett.*, vol. 104, p. 231112, 2014.

[108] C. Yang *et al.*, "Compact multilayer film structure for angle insensitive color filtering," *Sci. Rep.*, vol. 5, p. 9285, 2015.

[109] K. T. Lee, S. Y. Han, and H. J. Park, "Omnidirectional Flexible Transmissive Structural Colors with High-Color-Purity and High-Efficiency Exploiting Multicavity Resonances," *Adv. Opt. Mater.*, vol. 5, no. 14, p. 1700284, 2017.

[110] Z. Li, S. Butun, and K. Aydin, "Lithography-free transmission fi lters at ultraviolet frequencies using ultra-thin aluminum films," *J. Opt.*, vol. 18, p. 065006, 2016.

[111] A. Ghobadi, H. Hajian, A. R. Rashed, B. Butun, and E. Ozbay, "Tuning the metal filling fraction in metal-insulator-metal ultra-broadband perfect absorbers to maximize the absorption bandwidth," *Photonics Res.*, vol. 6, no. 3, 2018.

[112] Y. Lin and W. Chen, "Perfect meta-absorber by using pod-like nanostructures with ultra-broadband, omnidirectional, and polarization-independent characteristics," *Sci. Rep.*, vol. 8, p. 7150, 2018.

[113] Z. Liu *et al.*, "Automatically Acquired Broadband Plasmonic-Metamaterial Black Absorber during the Metallic Film-Formation," *ACS Appl. Mater. Interfaces*, vol. 7, pp. 4962–4968, 2015.

[114] C. Yang *et al.*, "Compact Multilayer Film Structures for Ultrabroadband,

Omnidirectional, and Efficient Absorption," *ACS Photonics*, vol. 3, no. 4, pp. 590–596, 2016.

[115] S. He, F. Ding, L. Mo, and F. Bao, "Light Absorber with an Ultra-Broad Flat Band Based on Multi-Sized Slow-Wave Hyperbolic Metamaterial Thin-Films," *Prog. Electromagn. Res.*, vol. 147, pp. 69–79, 2014.

[116] D. Ji *et al.*, "Broadband absorption engineering of hyperbolic metafilm patterns," *Sci. Rep.*, vol. 4, no. 1, p. 4498, 2014.

[117] H. U. D. Eng, C. H. J. M. Athai, S. H. G. Angopadhyay, J. Ie, G. Ao, and X. I. Y. Ang, "Ultra-broadband infrared absorption by tapered hyperbolic multilayer waveguides," *Opt. Express*, vol. 26, no. 5, pp. 6360–6370, 2018.

[118] Y. Cui *et al.*, "Ultrabroadband light absorption by a sawtooth anisotropic metamaterial slab," *Nano Lett.*, vol. 12, no. 3, pp. 1443–1447, 2012.

[119] W. Xue, X. Chen, Y. Peng, and R. Yang, "Grating-type mid-infrared light absorber based on silicon carbide material," *Opt. Express*, vol. 24, no. 20, pp. 22596–22605, 2016.

[120] F. Ding, Y. Jin, B. Li, H. Cheng, L. Mo, and S. He, "Ultrabroadband strong light absorption based on thin multilayered metamaterials," *Laser Photonics Rev.*, vol. 8, no. 6, pp. 946–953, 2014.

[121] J. Wu, "Broadband light absorption by tapered metal-dielectric multilayered grating structures," *Opt. Commun.*, vol. 365, pp. 93–98, 2016.

[122] J. Zhou, A. F. Kaplan, L. Chen, and L. J. Guo, "Experiment and Theory of the Broadband Absorption by a Tapered Hyperbolic Metamaterial Array," *ACS Photonics*, vol. 1, pp. 618–624, 2014.

[123] A. Ghobadi *et al.*, "97 Percent Light Absorption in an Ultrabroadband Frequency Range Utilizing an Ultrathin Metal Layer: Randomly Oriented, Densely Packed Dielectric Nanowires As an Excellent Light Trapping Scaffold," *Nanoscale*, vol. 9, no. 43, pp. 16652–16660, 2017.

[124] A. L. L. In *et al.*, "Lithography-free thin-titanium-nanocone metamaterial perfect absorbers using ZnO nanostructures," *Opt. Mater. Express*, vol. 7, no. 10, pp. 3608–3617, 2017.

[125] "Lumerical Solut. Inc. http://www.lumerical.com/tcad-products/fdtd/." .

[126] A. Ghobadi, S. A. Dereshgi, H. Hajian, B. Bozok, and B. Butun, "Ultra-broadband , wide angle absorber utilizing metal insulator multilayers stack with a multi- thickness metal surface texture," *Sci. Rep.*, vol. 7, p. 4755, 2017.

[127] F. Ding, J. Dai, Y. Chen, J. Zhu, Y. Jin, and S. I. Bozhevolnyi, "Broadband near-infrared metamaterial absorbers utilizing highly lossy metals," *Sci. Rep.*, vol. 6, p. 39445, 2016.